COMAP Early Science. VI. A First Look at the COMAP Galactic Plane Survey

Thomas J. Rennie[1], Stuart E. Harper[1], Clive Dickinson[1], Liju Philip[2], Kieran A. Cleary[3], Richard J. Bond[4],
Jowita Borowska[5], Patrick C. Breysse[6], Morgan Catha[7], Roke Cepeda-Arroita[1], Dongwoo T. Chung[4,8], Sarah E. Church[9],
Delaney A. Dunne[3], Hans Kristian Eriksen[5], Marie Kristine Foss[5], Todd Gaier[2], Joshua Ott Gundersen[10],
Andrew I. Harris[11], Brandon Hensley[12], Richard Hobbs[7], Håvard T. Ihle[5], James W. Lamb[7], Charles R. Lawrence[2],
Jonas G. S. Lunde[5], Roberta Paladini[13], Timothy J. Pearson[3], Maren Rasmussen[5], Anthony C. S. Readhead[3],
Nils-Ole Stutzer[5], Duncan J. Watts[5], Ingunn Kathrine Wehus[5], and David P. Woody[7]
(COMAP Collaboration)

[1] Jodrell Bank Centre for Astrophysics, Alan Turing Building, Department of Physics and Astronomy, School of Natural Sciences, The University of Manchester, Oxford Road, Manchester, M13 9PL, UK; thomas.rennie@manchester.ac.uk
[2] Jet Propulsion Laboratory, California Institute of Technology, 4800 Oak Grove Drive, Pasadena, CA 91109, USA
[3] California Institute of Technology, 1200 East California Boulevard, Pasadena, CA 91125, USA
[4] Canadian Institute for Theoretical Astrophysics, University of Toronto, 60 St. George Street, Toronto, ON M5S 3H8, Canada
[5] Institute of Theoretical Astrophysics, University of Oslo, P.O. Box 1029 Blindern, NO-0315 Oslo, Norway
[6] Center for Cosmology and Particle Physics, Department of Physics, New York University, 726 Broadway, New York, NY, 10003, USA
[7] Owens Valley Radio Observatory, California Institute of Technology, Big Pine, CA 93513, USA
[8] Dunlap Institute for Astronomy and Astrophysics, University of Toronto, 50 St. George Street, Toronto, ON M5S 3H4, Canada
[9] Kavli Institute for Particle Astrophysics and Cosmology & Physics Department, Stanford University, Stanford, CA 94305, USA
[10] Department of Physics, University of Miami, 1320 Campo Sano Avenue, Coral Gables, FL 33146, USA
[11] Department of Astronomy, University of Maryland, College Park, MD 20742, USA
[12] Department of Astrophysical Sciences, Princeton University, Princeton, NJ 08544, USA
[13] Infrared Processing Analysis Center, California Institute of Technology, Pasadena, CA 91125, USA

Abstract

We present early results from the CO Mapping Array Project (COMAP) Galactic Plane Survey conducted between 2019 June and 2021 April, spanning $20° < \ell < 40°$ in Galactic longitude and $|b| < 1°.5$ in Galactic latitude with an angular resolution of $4'.5$. We present initial results from the first part of the survey, including the diffuse emission and spectral energy distributions of H II regions and supernova remnants (SNRs). Using low- and high-frequency surveys to constrain free–free and thermal dust emission contributions, we find evidence of excess flux density at 30 GHz in six regions, which we interpret as anomalous microwave emission. Furthermore we model ultracompact H II contributions using data from the 5 GHz CORNISH catalog and reject these as the cause of the 30 GHz excess. Six known SNRs are detected at 30 GHz, and we measure spectral indices consistent with the literature or show evidence of steepening. The flux density of the SNR W44 at 30 GHz is consistent with a power-law extrapolation from lower frequencies with no indication of spectral steepening in contrast with recent results from the Sardinia Radio Telescope. We also extract five hydrogen radio recombination lines (RRLs) to map the warm ionized gas, which can be used to estimate electron temperatures or to constrain continuum free–free emission. The full COMAP Galactic Plane Survey, to be released in 2023/2024, will span $\ell \sim 20°$–$220°$ and will be the first large-scale radio continuum and RRL survey at 30 GHz with $4'.5$ resolution.

Unified Astronomy Thesaurus concepts: Surveys (1671); H II regions (694); Supernova remnants (1667); Interstellar medium (847); Milky Way Galaxy (1054); Radio continuum emission (1340)

1. Introduction

Surveys of the Galaxy at radio frequencies ($\nu \lesssim 100$ GHz) offer a largely unobstructed view of the interstellar medium (ISM). For example, observations of atomic cold gas via the 21 cm (1.4 GHz) H I line can map the gas throughout the entire Galactic disk. Furthermore, radio data provide unique information on the Galaxy not easily seen at other wavelengths such as large radio loops (Planck Collaboration et al. 2016a; Dickinson 2018). Radio emission can be used to estimate star formation rates as well as to study the diverse range of Galactic objects such as supernova remnants (SNRs), H II regions,

planetary nebulae, and molecular clouds (e.g., Brunthaler et al. 2021).

At radio frequencies, continuum emission comes from three phases of the ISM (Draine 2011): (i) synchrotron emission produced by relativistic cosmic rays (mostly electrons) accelerated by the Galactic magnetic field, (ii) free–free emission from warm ($T_e \sim 10^4$ K) ionized gas, mostly around hot O/B stars, and (iii) thermal vibrational (and spinning dust) emission from cold ($T_d \sim 15$–20 K) dust grains. Observations of the radio continuum over a wide range of frequencies can be used to separate the various continuum emission mechanisms into their individual components—namely, synchrotron emission, free–free emission, spinning dust or anomalous microwave emission (AME), and thermal dust emission. This form of component separation has been an important aspect of cosmic microwave background foreground removal, which typically uses the different frequency (or sometimes spatial) response of

each component to allow them to be separated (Leach et al. 2008; Dunkley et al. 2009). For example, synchrotron emission typically has a steep falling spectrum[14] ($\alpha \approx -0.5$ to -1.0), while free–free emission has a flatter spectrum when in the optically thin regime at gigahertz frequencies (see Section 4.3, for details).

While synchrotron, free–free, and thermal dust emission are well understood at this point, discussions on the origin of spinning dust emission (or AME in general) are ongoing. The main carrier of this emission is thought to be polycyclic aromatic hydrocarbons (PAHs) due to their small size, significant dipole moments, and abundance within the ISM (Draine & Lazarian 1998; Dickinson 2018; Hensley et al. 2022). Yet several analyses have found little correlation between AME and PAH tracers (e.g., Tibbs et al. 2011; Vidal et al. 2011; Tibbs et al. 2012; Battistelli et al. 2015; Hoang et al. 2016), which suggests that this may not be the case. However, this does not necessarily mean that PAHs are not the carriers of AME because the observed lack of correlation may be due to different excitation physics of PAHs in different environments (Hensley et al. 2022); there might be very large and currently underappreciated differences in the emissivity of PAHs in different interstellar environments, for example. Alternatives, such as nanosilicates, have also been shown to be viable AME carriers (Hensley & Draine 2017) and nanodiamonds have also been reported to potentially carry spinning dust emission at least in some circumstellar environments (Greaves et al. 2018). Close comparisons between high angular resolution radio and infrared data remain an important way to identify AME carriers.

Large-scale, total-power Galactic radio surveys have up to now, for the most part, been conducted at frequencies of a few gigahertz or below (Haslam et al. 1982; Reich & Reich 1986; Jonas et al. 1998; Calabretta et al. 2014; Carretti et al. 2019). Even with the largest radio dishes, the angular resolution at these frequencies is modest—typically tens of arcminutes or larger. The Canadian Galactic Plane Surveys at 408 MHz and 1.4 GHz have combined single-dish data with interferometric data to achieve an angular resolution of $1'$ (Landecker et al. 2010; Tung et al. 2017). Similarly, the GLOSTAR survey combines Very Large Array (VLA) and Effelsberg data at 4–8 GHz to achieve subarcminute resolution (Brunthaler et al. 2021). At the K_a band (26–40 GHz) near 30 GHz, the only total-power surveys available are the full-sky maps from the Wilkinson Microwave Anisotropy Probe (WMAP; Bennett et al. 2013) and Planck (Planck Collaboration et al. 2020) with angular resolutions of $\approx 32'$. A 33 GHz interferometric survey using the Very Small Array (VSA) (Todorovic et al. 2010) had an angular resolution of $13'$ but only covered longitudes of $26°$–$46°$.

The lack of high-resolution radio data at high ($\gtrsim 10$ GHz) frequencies is due partly to the lack of sensitive receivers and partly to the difficulty of observing from the ground above a few gigahertz. The atmosphere becomes increasingly opaque due to strong absorption from water and oxygen in some bands —most notably, the 22 GHz water line and the 61 GHz oxygen line. Although interferometric observations are possible at these high radio frequencies (e.g., Arcminute Microkelvin Imager (AMI) at 12–18 GHz; Perrott et al. 2015), mapping diffuse emission on large angular scales is difficult or impossible. Only total-power imaging with single-dish telescopes can easily map the sky on larger angular scales. A focal plane array of detectors is therefore the ideal solution to mapping the Galaxy to higher frequencies. The CO Mapping Array Project (COMAP) Pathfinder is such an instrument.

Focal plane arrays are ideal for mapping large areas, allowing multiple independent observations of the sky to be made at once. This is especially important for ground-based observations at high frequencies ($\gtrsim 10$ GHz) due to increased noise levels from atmospheric contributions to the system temperature (T_{sys}), $1/f$ noise, and smaller beamwidths.

COMAP was primarily designed to map the highly redshifted CO emission for understanding star formation and galaxy evolution over cosmic time (e.g., Li et al. 2015). It uses a wide band covering 26–34 GHz with a total of 4096 channels, which provides sensitivity to the 115 GHz $J = 1 - 0$ CO line at $z = 3.4$–4.4. For Galactic observations, the large bandwidth and focal plane array of 19 detectors are ideal for mapping the large-scale 30 GHz continuum as well as some spectral lines, such as radio recombination lines (RRLs). The 26–34 GHz range is a particularly interesting choice for a Galactic survey. First, the Galaxy has never been surveyed at this frequency and angular resolution. Second, the relatively high frequency is ideal for quantifying star formation based on the level of free–free emission present (e.g., Murphy et al. 2010). At lower radio frequencies (~ 1 GHz and below) ultracompact H II (UCHII) regions are optically thick and therefore go undetected, while at 30 GHz the majority of sources will be in the optically thin regime (e.g., Kurtz et al. 1994). Third, AME, which is thought to be primarily due to spinning dust emission (Dickinson et al. 2018), has a peaked spectrum near 30 GHz. Therefore, the COMAP survey is an ideal tool to map the AME and study how it varies with interstellar environments. The complete survey, which will be made publicly available by 2023/24, will be a valuable resource for Galactic astronomers.

This paper is part of a series of papers from the COMAP collaboration (Cleary et al. 2022), which outline the instrument and operations, as well as the cosmological results and interpretation. We envisage a series of future papers from the Galactic survey, covering specific sources and areas of investigation, culminating in the release of the complete COMAP Galactic Plane Survey covering $\ell \sim 20°$–$220°$.

This paper is organized as follows. Section 2 gives an overview of the COMAP instrument and the observations, data processing, calibration, and map-making. Section 3 summarizes the various multifrequency ancillary data sets that are used in conjunction with the COMAP data. Section 4 describes the source extraction, the photometry used to produce the spectral energy distributions (SEDs) for bright sources in the map, and the SED model fitting. Section 5 presents the results including an overview of current COMAP maps (Section 5.1), correlations with other surveys (Section 5.2), UCHII analysis (Section 5.3), the SEDs of H II regions (Section 5.4), SNRs (Section 5.5), and RRLs (Section 5.6). Finally, in Section 6 we discuss the results obtained so far and conclude with a future outlook.

2. Instrument and Observation Overview

In this section we will give a brief overview of the instrument, observations, and data processing relevant to the COMAP Galactic Plane Survey. The data processing of the Galactic plane survey differs in several respects from that of

---

[14] All spectral indices in this paper are in flux density units ($S \propto \nu^{\alpha}$).

Table 1
Main Characteristics and Parameters of the COMAP Galactic Plane Survey

Parameter	Value
Frequency Coverage	26–34 GHz
Channel Bandwidth	2 MHz
Binned Bandwidth	1 GHz
System Temperature	30–44 K
Beam FWHM @ 30 GHz	4′.5
Beam Gain	40–70 Jy K^{-1}
Beam Efficiency	0.72 ± 0.01
Absolute Calibration Accuracy	3.2% ± 0.1%
Relative Calibration Accuracy	<1%
Galactic Longitude Range	20° < ℓ < 220°
Galactic Latitude Range	−2° < b < 2°

the cosmology survey as we wish to preserve the continuum emission. The primary differences are with respect to how time-correlated noise fluctuations ($1/f$ noise) are suppressed using high-pass filters (Section 2.3) and destriping map-making (Section 2.5), and the calibration of the data using astronomical sources (Section 2.4). An overview of the instrument and survey parameters is given in Table 1.

The final COMAP Galactic Plane Survey maps have eight frequency bands at 26.5, 27.5, 28.5, 29.5, 30.5, 31.5, 32.5, and 33.5 GHz. When describing the maps in later sections we will refer to the 30.5 GHz map for comparisons with other data; however all eight bands are used when fitting the SEDs of the sources discussed in Section 5. Note that throughout this paper we use 30 GHz when referring to the 30.5 GHz COMAP data.

2.1. Instrument

Observations for the COMAP Galactic Plane Survey were made using the COMAP Pathfinder telescope (Lamb et al. 2022), sited in Owens Valley Radio Observatory (OVRO) in California. The telescope itself is of Cassegrain design and has an FWHM beamwidth of 4′.5 consistent to ±4% across 26–34 GHz (Lamb et al. 2022). The Pathfinder has a focal plane array of 19 forward-facing pixels in a hexagonal pattern. Feed centers are separated by 65 mm giving a sky-angle offset between pixels of 12′.04 and allowing for 19 independent observations of the sky to be taken simultaneously.

The radio frequency signal from each feed is passed into a polarizer, which converts the left-circular wave into linear polarization accepted by a low-noise amplifier operating at 15–18 K. The outgoing noise wave from the amplifier has its polarization reversed on reflection by the secondary and therefore does not couple back to the amplifier to cause a ripple in the spectrum. The amplifier output is then down-converted in two stages. The first mixes the 26–34 GHz with a 24 GHz local oscillator (LO), producing the first intermediate-frequency signal at 2–10 GHz. This is split into two paths, one feeding a 2–6 GHz filter (band A), and the other a 6–10 GHz filter (band B). Band A is mixed with a 4 GHz LO to produce an in-phase (I) and a quadrature (Q) signal at 0–2 GHz. Each of these baseband signals is sampled in an 8 bit analog-to-digital converter and the I and Q signals are combined in a field-programmable gate array (FPGA) to produce the lower sideband (LSB) of the 4 GHz LO at 2–4 GHz, and the upper sideband (USB) at 4–6 GHz. Similarly, band B uses an 8 GHz LO to convert to the I and Q basebands, converted by an FPGA to produce the 6–8 GHz and 8–10 GHz sidebands. The four

signals—LSB:A, USB:A, LSB:B, and USB:B—correspond to four continuous 2 GHz bands between 26 and 34 GHz on the sky.

The FPGAs then perform spectral analysis on 1024 channels for each 2 GHz band, with 2 MHz spectral resolution across the full 8 GHz bandwidth observable with COMAP. For a more complete description see Lamb et al. (2022). The resulting data set is collated alongside pointing, environmental, and house-keeping data and stored locally at Caltech.

2.2. Observations

The COMAP Galactic Plane Survey will cover the Galactic plane over the range $20° < ℓ < 220°$ in longitude and $−2° < b < 2°$ in latitude. Observations started in 2019 June and are ongoing. Typically 1–2 hr per day of COMAP observing time is dedicated to the Galactic plane survey. Since 2019 June we have surveyed $20° < ℓ < 50°$ in Galactic longitude, totaling 834 hr of observing time. Observations are initially calibrated at the beginning and end of each observation using a thermal load with a known temperature (details in Foss et al. 2022) and then calibrated to an astronomical brightness scale using daily observations of the SNR Taurus A/Crab Nebula (Tau A; Section 2.4). All observations were taken during the day.

The survey was conducted by observing the Galactic plane in discrete patches, where each patch covers an area of approximately 4 deg^2. As the COMAP instrument focal plane spans approximately ∼1°, we nested neighboring patches to ensure a uniform sensitivity across the survey. To map out each patch we would begin scanning the telescope in the horizon frame with a Lissajous pattern, and allow the natural rotation of the sky to move the patch center through the field of view of the telescope. The Lissajous scanning strategy traces sinusoidal patterns in the azimuth and elevation that result in each pixel in the celestial frame being visited by many different scan paths, a condition that is required for the map-making method (Section 2.5) as it allows for the true sky signal and correlated noise to be separated.

The Lissajous pattern is defined by the pair of equations

$$\delta_A = \frac{R}{\cos(E)} \sin(\omega_A t + \phi), \tag{1}$$

$$\delta_E = R \sin(\omega_E t), \tag{2}$$

where δ_A and δ_E represent the offset in azimuth and elevation from the central azimuth (A) and elevation (E) coordinates, ω_E and ω_A are the angular velocities along each axis, R is the radius of the scans, and ϕ is the relative phase. We used $R = 0°.8$ for the entire survey, the phase was alternated between $\pm\frac{\pi}{2}$, and the ratio of the angular velocities was randomly selected in the range $0.6 < \omega_E/\omega_A < 1$. The telescope was driven close to its maximum rate in elevation ($V_E^{max} = 0°.5 \text{ s}^{-1}$) for all observations. We modulated the Lissajous pattern by changing the azimuth scan speed ($V_A^{max} = 1° \text{ s}^{-1}$).

2.3. Data Processing

The nominal on-sky system temperatures were measured to be in the range 30–44 K across the full 26–34 GHz COMAP band. We rejected a number of channels that had abnormally high system temperatures caused either by spectral aliasing at the edges of the bands or by resonances within the feed optics

(see Lamb et al. 2022). After flagging bad channels, we averaged the native 2 MHz channels into wide 1 GHz bands.

When using the COMAP system for continuum science, the data are contaminated by substantial time-correlated noise (often referred to as $1/f$ noise; Harper et al. 2018) from two sources: fluctuations in the precipitable water vapor content in the atmosphere above the telescope, and small fluctuations in the gain or system temperature of the receiver low-noise amplifiers. Mitigating $1/f$ noise is critical to recovering the large-scale, diffuse Galactic structures and to achieving the lowest possible noise levels in the map. The strongest atmospheric $1/f$ noise can be mitigated by discarding data from days that have either poor or turbulent weather conditions. These can be determined by measuring the feed-to-feed noise correlation (as near-field atmospheric fluctuations will be strongly correlated between feeds), tracking the optical depth of the atmosphere using sky dips (Rohlfs et al. 2013), and measuring the power spectrum of the data to determine $1/f$ noise properties. We identified the very worst observations where the atmospheric fluctuations were several times the white noise of the receiver at timescales of 10 s or more and removed them, cutting the total optical depth (TOD) for all eight channels. This amounted to cutting approximately 17% of the observations, which were found to contain severe atmospheric contamination.

There is some contamination of the data from ground emission due to the local mountain ranges that lie to the east and west of OVRO. We characterized the ground emission profiles by performing 360° azimuth sweeps at fixed elevations. From these observations we could determine that the scale size of the ground emission is $\gg 1°$, much larger than the typical patches observed. On the scale of a single scan (the period between two repointings, i.e., $\approx 1°$; Foss et al. 2022) we approximated the ground emission (and other azimuth-correlated systematics) using a linear slope in azimuth, which gave a median amplitude for the ground emission across the survey of ≈ 6 mK. This ground emission slope was then subtracted from the TOD.

To suppress any remaining large-timescale $1/f$ noise fluctuations we used a running median filter with a scale size of 100 s (approximately equal to the typical time needed to complete a full scan—Section 2.2). Finally, we used the destriping map-making technique (see Section 2.5) in combination with the observing strategy to suppress $1/f$ noise down to timescales of 1 s.

2.4. Calibration

Calibration of the COMAP Galactic Plane Survey is done in two steps. First we calibrate the data using a calibration vane, a remotely controlled microwave absorber acting as a thermal load that covers the feed array at the beginning and end of each observation (i.e., approximately every 40 minutes). We take the difference between the known vane temperature ($T \approx 290$ K) and the cold sky ($T \approx 2.7$ K) to estimate both the system temperature and the total gain of the receiver and antenna system. The vane calibration procedure is described in Foss et al. (2022).

The effect of atmospheric absorption at 30 GHz is significant. We track atmospheric opacities using sky dips, which involve slewing the telescope between elevations of 40° and 60° over a period of a few seconds. We find that the typical opacity of the atmosphere at OVRO is in the range

$\tau \sim 0.07$–0.09, which equates to 15% absorption at 30° elevation. The vane calibration procedure corrects for atmospheric absorption due to the atmosphere along the line of sight. After the vane calibration we estimate the residual optical depth using the vane-calibrated observations of Tau A and Cassiopeia A (Cas A), and find the residual effect of atmospheric absorption to be $\delta\tau \sim 0.02 \pm 0.01$, which equates to a 2%–3% residual uncertainty in the calibration at the elevations used for the COMAP Galactic Plane Survey.

Absolute calibration to the main beam brightness scale is done using Tau A. We observe Tau A once per day and fit the peak brightness using a 2D Gaussian model. We derive the absolute calibration from the Tau A measurements by comparing them with the WMAP spectral fits and secular decrease models of Tau A (Tables 16 and 17 of Weiland et al. 2011). We do not apply color corrections when calculating model fluxes to calibrate on, as these are $\ll 1\%$ in each 1 GHz band. We verify the absolute calibration using Cas A and Jupiter and find an overall accuracy of 3.2% with a relative calibration between bands of $<1\%$. Models for Cas A are also taken from Weiland et al. (2011). The flux density model of Jupiter is derived by fitting a power law to the brightness temperature measurements taken using the CARMA instrument between 27 and 33 GHz (Karim et al. 2018), and using the ephemeris of Jupiter to track its solid angle on the sky. We combine these errors in quadrature giving an approximate 5% error on each of the eight maps in this work.

The COMAP beam has very good main beam isolation with the first sidelobe at more than 20 dB below the main beam response. Although this may be good enough in terms of confusion of nearby bright sources, these sidelobes still result in a scale-dependent calibration (see, e.g., Du et al. 2016, for a discussion of this issue). To estimate the level of the effect we radially integrate the COMAP beam models described in Lamb et al. (2022) out to the first null (i.e., the main beam) and third sidelobe (approximately $30'$ from the line of sight). We find that the integrated power changes by 10% between the main beam and $30'$ ($\approx 6\times$ the beam FWHM). For these early results we are largely interested in sources that are either unresolved or only partially resolved by the main beam, so the effect of beam dependence in this work is minimal.

2.5. Map-making

In order to suppress spurious large-scale contamination and any remaining $1/f$ noise within the COMAP continuum data we have implemented a bespoke destriping map-maker using the methods outlined in Delabrouille (1998), Sutton et al. (2009), and Sutton et al. (2010). Destriping map-making solves for $1/f$ noise by fitting linear offsets to the time-ordered data, but uses the scanning information to separate the $1/f$ noise from the true sky signal. To illustrate how destriping map-making works we will define the following data model:

$$d = Pm + Fa + n_w, \qquad (3)$$

where d is a vector containing the time-ordered data (for a single band, i.e., one time stream), m is the true sky signal, P maps the sky signal to the time domain, a represents the offsets that describe the $1/f$ noise, F maps these offsets to d, and finally n_w is the uncorrelated white noise vector.

Solving for the offsets in Equation (3) results in

$$\hat{a} = (F^T Z^T n^{-1} Z F)^{-1} F^T Z^T n^{-1} Z d, \qquad (4)$$

Table 2
Data Sets Used for SED Extraction, alongside Their Sky Coverage, Assumed Calibration Error, and Native Resolutions

Survey	Frequency (GHz)	Calibration Error (%)	Coverage	Resolution (′)	References
Effelsberg	2.7	10	$357° < \ell < 240°$, $\|b\| < 5°$	4.3	Reich et al. (1984), Reich et al. (1990), Furst et al. (1990)
Parkes	5.0	8	$190° < \ell < 40°$, $\|b\| < 2°$	4.3	Haynes et al. (1978)
Nobeyama	10.0	10	$10° < \ell < 50°$, $\|b\| < 1°$	2.7	Handa et al. (1987)
COMAP	26.5	5	$20° < \ell < 40°$, $\|b\| < 2°$	4.5	*This work*
COMAP	27.5	5	$20° < \ell < 40°$, $\|b\| < 2°$	4.5	*This work*
COMAP	28.5	5	$20° < \ell < 40°$, $\|b\| < 2°$	4.5	*This work*
COMAP	29.5	5	$20° < \ell < 40°$, $\|b\| < 2°$	4.5	*This work*
COMAP	30.5	5	$20° < \ell < 40°$, $\|b\| < 2°$	4.5	*This work*
COMAP	31.5	5	$20° < \ell < 40°$, $\|b\| < 2°$	4.5	*This work*
COMAP	32.5	5	$20° < \ell < 40°$, $\|b\| < 2°$	4.5	*This work*
COMAP	33.5	5	$20° < \ell < 40°$, $\|b\| < 2°$	4.5	*This work*
Planck HFI (DR3.1)	353	0.78	all-sky	4.8	Planck Collaboration et al. (2020)
Planck HFI (DR3.1)	545	6.1	all-sky	4.7	Planck Collaboration et al. (2020)
Planck HFI (DR3.1)	857	6.2	all-sky	4.3	Planck Collaboration et al. (2020)
Akari (160 μm)	1875	8.9	all-sky	1.5	Doi et al. (2015), Takita et al. (2015)
Akari (140 μm)	2143	8.9	all-sky	1.5	Doi et al. (2015), Takita et al. (2015)
IRAS (IRIS) Band 4 (12 μm)	3000	13.5	all-sky	4.3	Miville-Deschenes & Lagache (2005)
Akari (90 μm)	3333	5.7	all-sky	1.0	Doi et al. (2015), Takita et al. (2015)

where $\hat{\boldsymbol{a}}$ is the maximum-likelihood estimate of the offsets, and $\boldsymbol{n} = \langle \boldsymbol{n}_w \boldsymbol{n}_w^T \rangle$ is the white noise covariance matrix. The matrix $\boldsymbol{Z}$ is defined as

$$\boldsymbol{Z} = \boldsymbol{I} - \boldsymbol{P}(\boldsymbol{P}^T \boldsymbol{n}^{-1} \boldsymbol{P})^{-1} \boldsymbol{P}^T \boldsymbol{n}^{-1}. \qquad (5)$$

The COMAP Galactic Plane Survey maps use a plane cylindrical polar projection in the Galactic coordinate frame. The nominal offset length used to destripe the data was 1 s, which corresponds to approximately $18'$ scales on the sky. Our destriping map-maker suppresses the $1/f$ noise by a factor of four or better on scales up to $30'$. The average noise level of the final maps is 4.6 ± 1.2 mK arcmin^2.

3. Ancillary Data

Ancillary data were used from a variety of single-dish experiments between 408 MHz and 25 THz ($\lambda = 12 \mu$m). Spectral models were only fitted to flux densities below 3 THz ($\lambda = 100 \mu$m) as higher frequencies are contaminated by stochastic heating and emission from PAHs, which cause higher fluxes than would be naively expected from the simple models described in Section 4. In addition some frequencies were not fitted due to contamination from spectral lines, such as the Planck 100 and 217 GHz channels (contaminated by Galactic CO lines). A summary of the data sets used in this work is given in Table 2.

3.1. Map Preparation

The map-space processing was done using a custom-designed Python pipeline that operates in two steps: preparing and smoothing the maps, and then performing source extraction and photometry. This process began with any map-specific processes (such as reprojection or beam correction) and was then followed by two common final preparation steps in all maps.

In order to account for different beam sizes the data were smoothed to a common resolution—in this analysis, $5'$. The

units of each map were also converted to a common unit (MJy sr^{-1}) to allow easy extraction of integrated flux densities, and to allow maps to be readily compared side by side.

3.2. Ancillary Maps

3.2.1. Low-frequency Data Sets

Beginning at low frequencies, we used the Effelsberg Galactic plane survey 2.7 GHz ($\lambda = 11$ cm) maps, with associated 10% calibration error (Reich et al. 1984; Furst et al. 1990; Reich et al. 1990). This calibration was based on three point sources—two Seyfert 1 galaxies (3C 286 and 3C 138) and the quasar 3C 48—and large-scale gradients were removed by comparison with the Stockert survey (Reich & Reich 1986).

We also used the Parkes 5 GHz Galactic plane survey (Haynes et al. 1978) to constrain the free–free contributions to the overall source SEDs. For calibration we took the stated 8% accuracy based on measurements of Hydra A (assumed to be 13 Jy). In order to further verify this and ensure a reasonable calibration on scales greater than those of the beam (to be able to judge the source morphology etc.) we smoothed the Parkes and the Sino-German survey (Gao et al. 2019) to $10'$ resolution and performed T–T plot analysis (e.g., Davies et al. 1996) on the Galactic plane within $20° < \ell < 40°$ for Galactic latitudes less than $|b| < 2°$, masking out bright point sources, and fitting for a gradient between the maps of (0.98 ± 0.03) consistent with a one-to-one ratio. Since both surveys are comparable single-dish 5 GHz surveys, a gradient consistent with 1 confirms both that Parkes is correctly calibrated, and that the diffuse structures seen in the Sino-German survey are present in the Parkes 5 GHz data.

For the 10 GHz data points we incorporated the Nobeyama FUGIN Galactic plane survey (Handa et al. 1987). The survey was ideally placed for this analysis with a slightly smaller beamwidth of $2.'7$ than COMAP on a single-dish telescope. No formal calibration uncertainties were given in Handa et al. (1987);

we adopted a 10% calibration uncertainty, which resulted in reasonable χ^2 values for the fitted SED models (Section 5.4).

It should be noted that the Canadian Galactic Plane Survey (Taylor et al. 2003) at 1.4 GHz was not included in our analysis despite having arcminute resolution. This was because the survey does not cover the longitude range analyzed in this work, but it will be valuable for future analyses at higher longitudes ($\ell > 58°$).

3.2.2. High-frequency Data Sets

Including the Planck High Frequency Instrument (HFI) bands to fill in the thermal dust emission was vital to understanding the sources presented in this work. Full-mission maps were used for the analysis presented, and were sourced from the Planck Legacy Archive.[15] Maps from Planck HFI bands were convolved to a 5′ Gaussian beam using the HFI beam models (see Planck Collaboration et al. 2014a, for details) and then reprojected from HEALPix (Gorski et al. 2005) to a Cartesian grid. Due to the high resolution of the HEALPix maps retrieved and our later need to further smooth the maps we did not see significant pixelization effects when comparing the Planck data against other ancillary data sets. We also used color correction as described by Planck Collaboration et al. (2014b) for the HFI, which was accounted for in the Markov Chain Monte Carlo (MCMC) fitting. Furthermore we used the calibration errors provided in Planck Collaboration et al. (2014b), which gave calibration errors between 0.09% and 6.4% for the HFI.

Due to the beamwidth of the Planck instrument being significantly larger at lower frequencies, we were only able to employ the HFI bands above 217 GHz for this analysis. This unfortunately meant that we had no surveys between the upper COMAP band (33.5 GHz) and the 217 GHz Planck band to aid the fitting of the AME component.

While we included all the data points in the SED plots, we did not use the Planck 217 GHz band in fitting since these bands are affected by Galactic CO(1–0) and CO(2–1) transitions. In future work we will attempt to include these frequencies by subtracting the Planck internal estimate of Galactic CO emission (Planck Collaboration et al. 2014c).

Finally, we utilized Akari (Doi et al. 2015) and IRIS (Miville-Deschenes & Lagache 2005) data to fill in the terahertz frequencies. These maps were sourced via the CADE archive, retrieved in HEALPix, and then converted to a Cartesian grid. As seen in Table 2 we did not use all the terahertz maps for SED fitting due to stochastic heating within the dust cloud taking effect at frequencies higher than that of the modified blackbody peak. For this purpose, we found that placing a limit at 3000 GHz allowed for enough data points to be included such that the modified blackbody was sufficiently constrained but that we did not include the more complex reemitted radiation (see in-depth discussion in Compiegne et al. 2011). For the two surveys we took calibration errors from their respective papers as reported in Table 2 giving values between 5.7% and 8.9% for Akari and a value of 13.5% for IRAS band 4.

4. Source Selection and SED Model Fitting

For our early analysis, we performed source extraction and SED fitting to a number of H II regions and SNRs. For H II regions we utilized a source extraction and aperture photometry pipeline as described in Sections 4.1 and 4.2. For SNRs we fit apertures and annuli by eye and then run them through the aforementioned aperture photometry pipeline.

4.1. Source Extraction

The first task required identifying bright, relatively compact sources within a small sample region of the COMAP survey for early analysis. We focused on sources that can be measured easily due to their brightness relative to their background, and their compact size relative to that of the beam, i.e., $\lesssim 5′$. To do this the COMAP 30 GHz map was put through the preparation described in 3.1 and then through a Python implementation of Source Extractor Python (SEP; Barbary 2016), a Python wrapper for SExtractor (Bertin & Arnouts 1996).

Within the SEP implementation several options were invoked to ensure a reliable source list was returned which minimized the number of false detections. The first process used was filtering—this was done with an unnormalized Ricker wavelet of the form

$$f_{\mathrm{MH}}(r, \sigma) = \left(1 - \frac{1}{2}\frac{r^2}{\sigma^2}\right)\exp\left\{-\frac{1}{2}\frac{r^2}{\sigma^2}\right\}, \qquad (6)$$

where r represents the radius from the center of the filter, and σ represents the filter's standard deviation. The filter was computed on a 15×15 array (which equates to a $15′ \times 15′$ space when projected onto the map) with a standard deviation of 2.2 to match the COMAP beam.

When inputting a signal-to-noise cutoff into SEP, we found that the influence of the diffuse background and the high density of sources caused the noise estimates to be greater than those measured by using an aperture on the background by an order of magnitude. As such, we input a measured background noise level of 6.5 ± 2.4 mK on scales of $15′$ and applied a 5σ detection limit on all sources.

After this analysis of the raw COMAP 30 GHz map 21 candidate sources were identified. Through checking each source by eye in all eight COMAP bands and the 5 GHz Parkes and Planck maps, sources were either verified or rejected. These sources were verified by a clear detection in all eight COMAP bands in addition to a clear detection in one of the two other maps (verifying a strong dust and/or free–free component from the source). However, performing photometry on some of these remaining sources was still nontrivial. We therefore further removed additional sources that were still weak and if the background was sufficiently bright/complicated those whose flux densities were not robust to variation in the background annulus locations. This left a total of nine sources with robust SEDs to present in Section 5.4.

4.2. Aperture Photometry

We used aperture photometry to measure the flux densities of the sources identified in the previous section. While we see that Gaussian fitting may be more suited to such a complex region as the Galactic plane, particularly for sources embedded within extended emission, we implement a simple aperture photometry technique here to provide an early indication of the

spectral composition of such sources on small scales. Since we are focused on brighter sources, aperture photometry should provide a reliable estimate of the flux density.

For the H II regions, we used a constant aperture radius of $r = 5'(1\sigma)$ to integrate the flux of each source. We found this to be suitable given that each source on the initial extracted list had a fitted standard deviation in the range $2'.2 < \sigma < 2'.5$, giving a $\approx 2\sigma$ aperture radius size. For background measurements we used an annulus drawn between $6'.7$ and $8'.3$ from the source coordinates and used the median pixel value to estimate a background that was robust against nearby bright sources.

In the case of SNRs, we treated these separately due to the large amount of variability between sources, and the tendency of SNRs to appear as extended sources. For these sources we did not perform a specific source extraction, but used the values given in Green (2019) to set initial values for the radius and central coordinates of the aperture and annulus used, adjusting these to fit the SNRs as they appeared in the maps and the background. We then used the adapted central coordinates and radii in the aperture photometry pipeline in Section 4.2 to obtain flux measurements from our maps.

4.3. SED Fitting

We fit the flux density of each H II source measured using aperture photometry (Section 4.2) with a three-component model of the free–free (S_{ff}), thermal dust (S_{td}), and AME components (S_{AME}):

$$S = S_{ff} + S_{td} + S_{AME}. \tag{7}$$

We modeled the free–free emission flux density by first calculating the free–free brightness temperature and converting it to flux density units via

$$S_{ff} = \frac{2k_B T_{ff} \Omega_{beam} \nu^2}{c^2}, \tag{8}$$

where k_B represents the Boltzmann constant, Ω_{beam} the beam solid angle, ν the frequency, and c the speed of light. T_{ff} is defined as (e.g., Draine 2011)

$$T_{ff} = T_e(1 - e^{-\tau_{ff}}), \tag{9}$$

where T_e is the the electron temperature and τ_{ff} is the free–free emission optical depth:

$$\tau_{ff} = 5.468 \times 10^{-2} T_e^{-1.5} \nu^{-2} EM g_{ff}, \tag{10}$$

where g_{ff} is the Gaunt factor, which for these frequencies can be approximated as

$$g_{ff} = \ln\left(\exp\left[5.960 - \frac{\sqrt{3}}{\pi} \ln(\nu_{GHz} T_4^{-1.5})\right] + 2.71828\right), \tag{11}$$

where $T_4 = T_e \times 10^{-4}$. For the SED fitting we let the emission measure be a free parameter, while the electron temperature we fixed to a typical value of $T_e = 7500$ K (e.g., Paladini et al. 2003). However, the fit was only weakly dependent on the choice of T_e.

The thermal dust emission was modeled as a modified blackbody curve given by

$$S_{td} = 2h\frac{\nu^3}{c^2}\frac{1}{e^{h\nu/k_B T_d} - 1}\left(\frac{\nu}{353\,\text{GHz}}\right)^{\beta_d}\tau_{353}\Omega_{beam}, \tag{12}$$

and we fit for the optical depth of thermal emission at 353 GHz (τ_{353}), the dust temperature (T_d), and the emissivity spectral index (β_d). It is worth noting that there are well-known degeneracies between the emissivity spectral index and dust temperature (e.g., Dupac et al. 2003; Désert et al. 2008; Planck Collaboration et al. 2014).

We modeled the AME spectrum as a lognormal curve as this is a flexible model that is a good approximation to a spinning dust spectrum (Bonaldi et al. 2007; Stevenson 2014; Dickinson et al. 2018); it is defined as

$$S_{AME} = A_{AME} \exp\left\{-\frac{1}{2}\left(\frac{\ln(\nu) - \ln(\nu_{AME})}{w_{AME}}\right)^2\right\}, \tag{13}$$

where we fit for the amplitude of the AME (A_{AME}), the peak frequency (ν_{AME}), and the width of the lognormal (w_{AME}).

For the SNRs we did not fit for a free–free or AME component but instead fit for synchrotron emission (S_{sync}) so the SED model became

$$S = S_{sync} + S_{td}, \tag{14}$$

where the synchrotron component is modeled as a simple power law:

$$S_{sync} = A_{sync}\nu^{\alpha}, \tag{15}$$

where we fit for the spectral index of the synchrotron (α), and the synchrotron amplitude at 1 GHz (A_{sync}).

The SEDs were fitted using an MCMC analysis, and the emcee ensemble sampler (Goodman & Weare 2010; Foreman-Mackey et al. 2013a) as the backend. The implementation we used is the same as that described in Cepeda-Arroita et al. (2021) with a modification to account for the correlation in noise between the COMAP bands. For each fit we used 300 chains, each with 5000 steps. The burn-in time for each fit required between 1300 and 1400 steps as assessed by eye, and so we discarded the first 1500 from each chain. The typical correlation length of the samples was 390 steps, which we used to thin the chains and to suppress sample-to-sample correlations. We checked each chain for convergence, and discarded those that failed.

At the resolution of COMAP there are no surveys that cover the frequency range 40–100 GHz. The lack of data at these frequencies means that the peak and width of the AME lognormal are poorly constrained. To improve the convergence of the MCMC fitter we implemented Gaussian priors on ν_{AME} and w_{AME}. The Gaussian priors were informed by measuring the integrated flux density of W43 using the same $1°$ radius aperture and background annulus ($1°.3–1°.7$) used in Irfan et al. (2015) and Génova-Santos et al. (2017). By using maps smoothed to $30'$ resolution we were able to use the data sets in Table 2 alongside the lower-resolution Planck Low Frequency Instrument (LFI) 28.4, 44, and 70 GHz bands. Fitting for a model with free–free emission, AME, and thermal dust emission we constrained a mean peak frequency and lognormal width for the region. The final Gaussian priors we used for the H II SED fits were $N(28 \pm 15\,\text{GHz})$ for the peak frequency (ν_{AME}), and $N(0.6 \pm 0.2)$ for the width (w_{AME}).
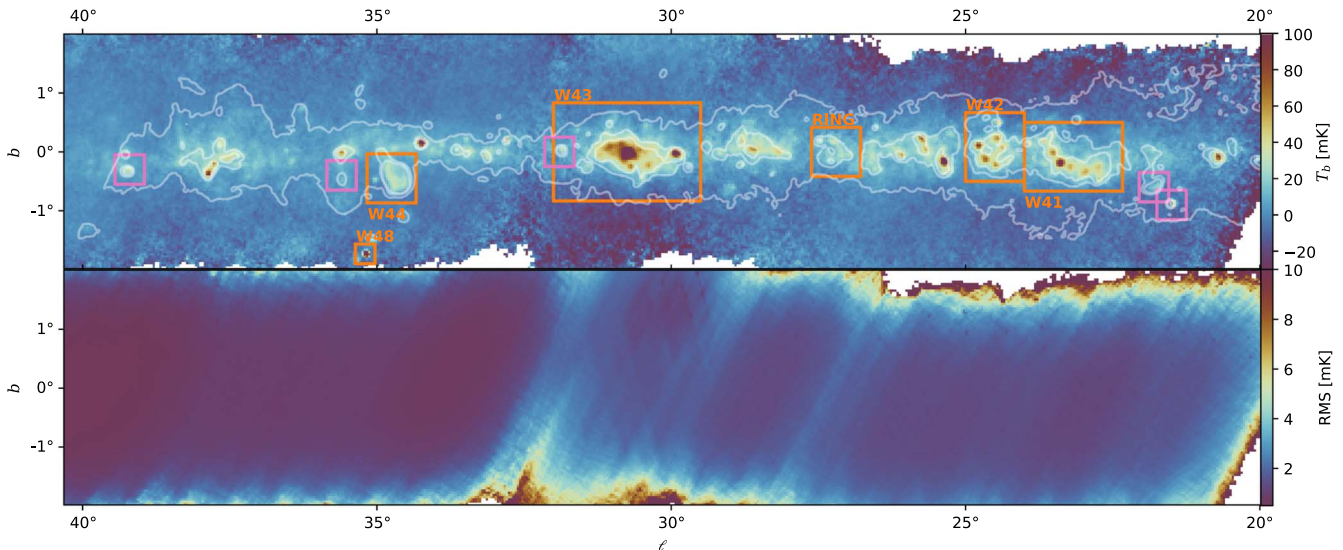
Figure 1. The current COMAP band-averaged 30 GHz map (top panel) covering the Galactic plane within $20° < \ell < 40°$. The color scale is linear and in units of brightness temperature (mK). Masked pixels are white. The bottom panel shows the coverage in terms of the local rms in the map. Westerhout complexes are indicated as *orange rectangles*, including the SNR W44. The other detected SNRs are indicated by *purple squares*. Contours are given for the Parkes 5 GHz Galactic plane survey at levels of 1, 1.5, and 2.0 MJy sr^{-1}.

5. Results

5.1. COMAP Survey Map

In Figure 1 we show the COMAP 30.5 GHz map covering $20° < \ell < 40°$ on the *top* panel, and the total number of integrations per 1′ pixel in the *bottom* panel. The map units are in millikelvins and the map has a resolution of 4.′5. We detect with a high signal-to-noise ratio (S/N) several bright giant molecular cloud regions such as G023.3−00.3 (e.g., Messineo et al. 2014) and W43 at $(\ell, b) = (25.°4, -0.°2)$ (e.g., Nguyen Luong et al. 2011); several giant H II regions such as G24.5 −0.0 and W42 at $(\ell, b) = (25.°4, -0.°2)$, as well as many known H II regions and H II complexes (e.g., Paladini et al. 2003; Anderson et al. 2014); and also several SNRs (Section 5.5). Besides discrete sources we detect extended emission in the form of diffuse structures and spurs. Most of the diffuse emission is caused by diffuse ionized gas formed from the leakage of ionizing radiation from nearby O/B stars into the ISM (Zurita et al. 2000), but there will also be dust-correlated AME due to spinning dust grains (Hensley et al. 2016; Dickinson et al. 2018) potentially contributing up to ≈20%–45% of the observed brightness (Planck Collaboration et al. 2011, 2015).

The map has a high S/N across much of the Galactic plane. The noise level of the map varies between 2 and 3 mK beam^{-1} away from the edges, or equivalently 0.1–0.15 Jy beam^{-1}. Due to the filtering of the time-ordered data on timescales corresponding to the typical scan length of ∼1°, the largest scales are not well constrained. We find that there is a loss of flux of 15% or more on scales larger than about 30′. For example, a comparison between the integrated flux density of W43 at 30′ resolution over a 2° diameter aperture in the COMAP 28.5 GHz data and that measured by the Planck LFI at 28.4 GHz (504 ± 26 Jy; Irfan et al. 2015) shows that we are underestimating the integrated flux density by ≈15%. However, as discussed in Section 2.4 the data have been calibrated to 5% or better at the main beam scale (taking into account both opacity errors and those on the raw calibration) out to a few
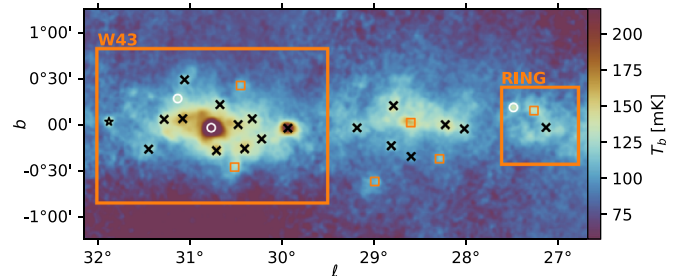

Figure 2. COMAP 30 GHz map of W43 showing the locations of sources extracted: H II regions found to fit best to a non-AME model (*white circles*), H II regions found to best fit a model with AME (*orange squares*), SNRs (*black stars*), and other sources detected but discounted from an SED analysis (*black crosses*). We also mark the W43 region and ring structure (referred to in Section 5.4.1) using *orange boxes*.

times the FWHM (∼12′); therefore we will primarily focus on discrete (i.e., clear, high-S/N) sources for this first analysis. In future releases we will use the COMAP beam models (Lamb et al. 2022) to deconvolve the map and use simulations to help improve the data processing in order to preserve large-scale structures.

In the following sections we will discuss several initial analyses of the COMAP Galactic Plane Survey. In Section 5.2 we will compare the pixel brightnesses of the diffuse emission at 30 GHz with surveys at 5 and 353 GHz. In Section 5.3 we discuss the general contribution of UCHII regions to the total emission observed at COMAP frequencies using data from the CORNISH survey UCHII catalog. In Section 5.4 we discuss nine H II regions selected from the COMAP Galactic Plane Survey and look for evidence of AME. In Section 5.5 we look at the fitted SEDs of six known supernovae (SNRs) over the full $20° < \ell < 40°$ range shown in Figure 1. Finally, in Section 5.6 we present preliminary detections of RRLs from both compact and diffuse ionized gas within the COMAP band within the area marked W43 in Figure 2.
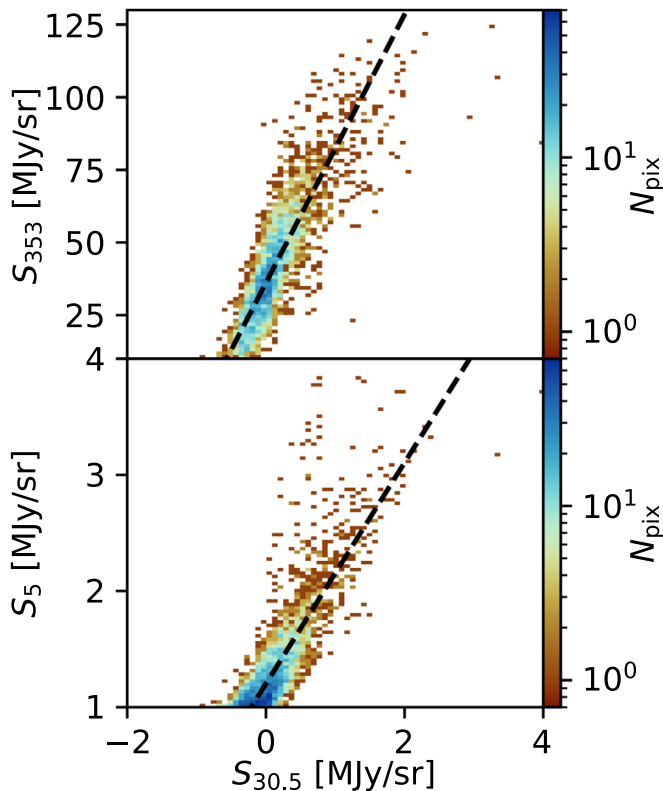
Figure 3. Binned T–T plots of pixel brightnesses of the COMAP 30 GHz data with the Parkes 5 GHz (top) and Planck 353 GHz (bottom) data. The *dashed* line shows the best-fitting linear model, the parameters of which are discussed in Section 5.2.

5.2. Correlation with Other Surveys

We begin the analysis with an initial look at the correlation of the diffuse emission seen at 30 GHz shown in Figure 1 with the 5 GHz Parkes map (primarily tracing free–free emission; Calabretta et al. 2014) and the 353 GHz Planck map (tracing dust emission; Planck Collaboration et al. 2020). We will derive the average spectral index and Pearson correlation coefficient of the diffuse emission between each frequency pair. If AME is present in the diffuse emission at 30 GHz we will expect to see a rising spectrum between 5 and 30 GHz that is greater than that predicted for free–free emission ($\alpha_{5-30} > -0.1$), and significant correlation between the 30 and 353 GHz data. We account for the possible filtering on large scales discussed earlier by including a conservative 15% calibration uncertainty on the COMAP data (due to the loss of flux density on large scales discussed in Section 5.1).

Before comparing the pixel brightnesses we first smooth all the data sets to a common resolution of $5'$ and change the pixel size to match the resolution of the maps to reduce pixel-to-pixel correlations in the noise. We then mask all pixels with a pixel brightness of less than 1 MJy sr^{-1} at 5 GHz; the mask area is shown by the lowest contour in Figure 1. We also mask the very brightest sources that exceed 6 MJy sr^{-1} at 30 GHz. The mask ensures we have good S/N in the majority of pixels and mitigates the possibility of including low-level large-scale modes that are not well constrained away from the Galactic plane.

In Figure 3 we compare the pixel brightness in the 5 GHz and 353 GHz maps with COMAP 30 GHz data. We can see there is a strong correlation between the 30 GHz data and both

5 GHz and 353 GHz emission. The Pearson correlation coefficient between each frequency pair is consistent: $r_{5-30} = 0.72$, $r_{30-353} = 0.68$, and $r_{5-353} = 0.70$. Strong correlations between all three bands are not unexpected near the Galactic plane as the complex dust and gas dynamics of these regions leads to significant mixing of ISM phases.

The dashed lines in Figure 3 show the best-fit linear relationships between the pixel brightnesses. We convert the fitted gradients into the spectral index between pairs of frequencies by

$$\alpha = \frac{\log\left(dS_{\nu_0}/dS_{\nu_1}\right)}{\log\left(\nu_0/\nu_1\right)}, \tag{16}$$

where α is the spectral index between frequencies ν_0 and ν_1.

The spectral index that we measure between 5 GHz and 30 GHz is $\alpha_{5-30} = 0.035 \pm 0.017$, which is inconsistent with the expected free–free spectral index of $\alpha_{\mathrm{ff}} \approx -0.1$ (Draine 2011) at the level of 7.9σ. It is possible for a rising spectrum between 5 and 30 GHz to be due to optically thick free–free emission from embedded UCHII regions, but as discussed in Section 5.3, we find that on average UCHII regions have a negligible impact on these angular scales at 30 GHz. We therefore interpret this excess as due to AME, probably in the form of spinning dust. We can estimate what fraction of the emission measured at 30 GHz is due to AME by

$$\eta_{\mathrm{AME}} = 1 - \frac{(\nu_1/\nu_0)^{-0.1}}{(\nu_1/\nu_0)^{\alpha_{5-30}}}, \tag{17}$$

where $\nu_1 = 30.5$ GHz, and $\nu_0 = 5$ GHz. We find a fractional AME of $\eta_{\mathrm{AME}} = (22 \pm 2)\%$. There have been several previous estimates of the AME fraction around 30 GHz. Planck Collaboration et al. (2011), using a template fitting method, estimated the AME fraction at 28.4 GHz to be $(25 \pm 5)\%$ across all longitudes, but found particular longitudes to have as high as 100%; however such high AME fractions are likely due to modeling errors in complex regions. Planck Collaboration et al. (2015) also performed a template fitting analysis but made use of RRL data over the range $5° < \ell < 60°$ and found an average AME fraction of $(45 \pm 1)\%$. Planck Collaboration et al. (2018) found the average AME fraction of individual bright AME regions is $(50 \pm 2)\%$.

In future work we will expand this analysis to a full correlation analysis where we jointly fit for emission components at 30 GHz using templates in a similar way to what has been done at lower resolutions (e.g., Davies et al. 2006). However, since the free–free emission and thermal dust emission are so strongly correlated ($r_{5-353} = 0.70$) such an analysis will require careful consideration of this correlation.

5.3. UCHII Regions

As described in Section 4.3, the SED fitting assumes that free–free emission may be fit by a single optically thin and spatially smooth component. Therefore any contribution from younger, compact H II regions with rising spectra and higher turnover frequencies may erroneously be classified as AME. These young compact H II regions can be further classified as UCHII and hypercompact H II (HCHII) regions depending on their electron density and emission measure (e.g., Churchwell 2002; Kurtz 2002). The most compact objects (UCHII/HCHII) can exhibit turnover at frequencies of tens of gigahertz

Table 3
Fitted SED Parameters for H II Sources Analyzed with Their Associated Geometric Mean Widths from Source Extraction (θ) and In-band Spectral Indices (α_{26-34})

| Source | | In-band | Thermal Dust | | | Free–Free | AME Lognormal | | | | |
Name	θ (′)	α_{26-34}	T_d (K)	β	$\log_{10}(\tau_{353})$	EM × 10^{-3} (pc cm^{-6})	A_{AME} (Jy)	ν_{AME} (GHz)	w_{AME}	ΔS_{30} (Jy)	$\epsilon_\nu \times 10^{18}$ (Jy sr^{-1} cm^2 H^{-1})
G027.488+00.199	4.5	$0.5^{\pm0.1}$	$30^{\pm3}$	$1.50^{\pm0.24}$	$-3.79^{\pm0.07}$	$12.7^{\pm0.4}$	...	...	...	<0.13	<1.25
G030.744−00.036	6.7	$-0.0^{\pm0.1}$	$22^{\pm1}$	$2.10^{\pm0.08}$	$-2.19^{\pm0.02}$	$398^{\pm14}$	...	...	...	<1.49	<0.5
G031.125+00.294	3.9	$-0.8^{\pm0.5}$	$27^{\pm4}$	$1.30^{\pm0.29}$	$-3.71^{\pm0.13}$	$5.3^{\pm0.4}$	...	...	...	<0.21	<2.8
G027.266+00.165	5.9	$0.8^{\pm0.1}$	$22^{\pm1}$	$2.02^{\pm0.16}$	$-3.56^{\pm0.05}$	$7.1^{\pm0.7}$	$1.0^{\pm0.5}$	$41^{\pm17}$	$0.81^{\pm0.21}$	$0.98^{\pm0.10}$	$10.1^{\pm3.8}$
G028.289−00.356	3.8	$0.1^{\pm0.1}$	$23^{\pm1}$	$2.03^{\pm0.16}$	$-3.40^{\pm0.05}$	$5.7^{\pm0.6}$	$0.6^{\pm0.4}$	$40^{\pm16}$	$0.73^{\pm0.23}$	$0.52^{\pm0.07}$	$9.2^{\pm3.5}$
G028.600+00.035	6.6	$0.4^{\pm0.1}$	$23^{\pm1}$	$1.79^{\pm0.12}$	$-3.14^{\pm0.03}$	$14.0^{\pm1.0}$	$1.2^{\pm0.3}$	$44^{\pm13}$	$0.71^{\pm0.20}$	$1.06^{\pm0.11}$	$3.3^{\pm1.2}$
G029.038−00.636	12.1	$0.4^{\pm0.1}$	$27^{\pm2}$	$1.70^{\pm0.19}$	$-3.35^{\pm0.05}$	$17.5^{\pm1.2}$	$3.6^{\pm1.0}$	$47^{\pm10}$	$0.56^{\pm0.13}$	$1.97^{\pm0.14}$	$3.0^{\pm1.1}$
G030.443+00.435	6.1	$1.0^{\pm0.2}$	$22^{\pm2}$	$1.66^{\pm0.24}$	$-3.34^{\pm0.06}$	$5.2^{\pm0.5}$	$0.9^{\pm0.3}$	$47^{\pm13}$	$0.59^{\pm0.20}$	$0.70^{\pm0.08}$	$3.2^{\pm1.2}$
G030.508−00.447	4.9	$0.4^{\pm0.1}$	$23^{\pm2}$	$1.73^{\pm0.23}$	$-3.35^{\pm0.05}$	$6.9^{\pm0.8}$	$1.1^{\pm0.4}$	$45^{\pm14}$	$0.66^{\pm0.22}$	$0.89^{\pm0.10}$	$8.3^{\pm3.1}$

Note. The fitted parameters are given for the models discussed in Section 4; the model excess emission (ΔS_{30}) and emissivity at 30 GHz (ϵ_ν) are calculated from the excess and optical depth at 353 GHz. For non-AME sources we present 2σ upper limits on the last two parameters: 30 GHz excess and emissivity.

(Kurtz 2002), although the flux density of individual objects will typically be low (∼mJy). In this section we describe the average contribution of UCHII regions to the emission at 30 GHz.

To account for these contributions, one would ideally like to survey at high frequency (e.g., 30 GHz) *and* high angular resolution (∼arcsec) to allow each source to be accounted for (each source will typically be quite weak—typically at the level of tens to hundreds of millijanskys). Unfortunately while COMAP does have the required frequency coverage, it does not have the angular resolution necessary to perform such a search; however we may consult external catalogs to search for compact sources that may influence our findings. The most appropriate survey to date is the 5 GHz CORNISH VLA radio survey (Hoare et al. 2012) of the northern Galactic plane. We use the UCHII catalog from the 5 GHz CORNISH survey (Purcell et al. 2013; Kalcheva et al. 2018). The CORNISH survey catalogs ∼3000 sources in total at 5 GHz with 1″.5 resolution, 54 of which lie within our survey area of $20° < \ell < 40°$. Considering that we report 30 GHz excess fluxes of ≈1 Jy, we would typically require ∼100 UCHII regions to account for the excess flux observed.

The catalog is estimated to be 90% complete to point sources at 3.9 mJy but is less complete for extended emission, resolving out sources larger than 14″. However, these extended H II regions will, by definition, have lower densities and therefore lower turnover frequencies, i.e., they will not be UCHII regions and are therefore less likely to contribute to the excess emission at ∼30 GHz.

All the sources in the CORNISH UCHII catalog were classified based on their morphological and positional similarity to IR counterparts in the 8 μm band of the GLIMPSE survey (Kalcheva et al. 2018; GLIMPSE Team 2020). Proximity to IR clusters and dust lanes was used to distinguish UCHII regions from other objects meeting the above criteria such as massive young stellar objects and planetary nebulae.

We have assessed the contribution from the 54 cataloged UCHII sources to the fitted AME and found it to be negligible. However, we must also consider the potential for sources that were not included in the catalog to make a significant contribution. These sources fall into two main categories: (i) any compact H II sources that appeared in the parent CORNISH catalog but were not detected in GLIMPSE (referred to as "IR-quiet") and so could not be classified as

UCHII regions, and (ii) sources falling below the completeness level of the parent CORNISH catalog.

Of the CORNISH IR-quiet sources 80% have flux densities of ⩽13 mJy. Therefore, we conservatively estimate the contribution of sources missing from the catalog by assuming a true completeness level of the UCHII catalog of 13 mJy (over three times the point-source completeness limit of the CORNISH survey).

Yang et al. (2021) observed 116 young H II regions that have rising spectra from 1 to 5 GHz (5 in our survey area), and found 20 sources with turnover frequencies >5 GHz (4 in our survey area), with maximum and mean turnover frequencies of 16.7 GHz and 9.7 GHz, respectively. If we consider a source with a 5 GHz flux density of 13 mJy and assume the source to have the maximum turnover frequency ($\nu_t = 16.7$ GHz) reported by Yang et al. (2021), its 30 GHz flux density is just ∼13% of the mean excess (ΔS_{30} in Table 3). This contribution decreases significantly to ∼4% if we assume the source to have the mean turnover frequency ($\nu_t = 9.7$ GHz).

Given the rarity of UCHII regions with such high turnover frequencies, we conclude that sources missing from the CORNISH UCHII catalog do not make a significant contribution to the reported AME in this paper. The largest contribution in any of the sources initially found by our analysis is seen to be ≈4% although most sit well below this contribution. Nevertheless, as we expand the COMAP survey, there might be some lines of sight where UCHII regions, particularly if there is a cluster within a molecular cloud, could account for a major fraction of the total flux density. In Section 5.4 we also provide details on the UCHII region contributions to each of the six AME sources.

5.4. H II Region SEDs

At frequencies of $\nu < 100$ GHz H II regions are dominated by free–free emission, which has a well-defined spectral shape (Draine 2011) that at frequencies within $5 < \nu < 100$ GHz is often optically thin with a spectral index of $\alpha_{ff} \approx -0.1$. There are several examples of AME being detected in H II regions (Watson et al. 2005; Dickinson et al. 2007; Planck Collaboration et al. 2018), as well as observations associating the AME with the swept-up circumstellar material at the boundaries of H II regions (Tibbs et al. 2010, 2012; Cepeda-Arroita et al. 2021). However, not all H II regions show evidence of AME (Scaife et al. 2007, 2008). In
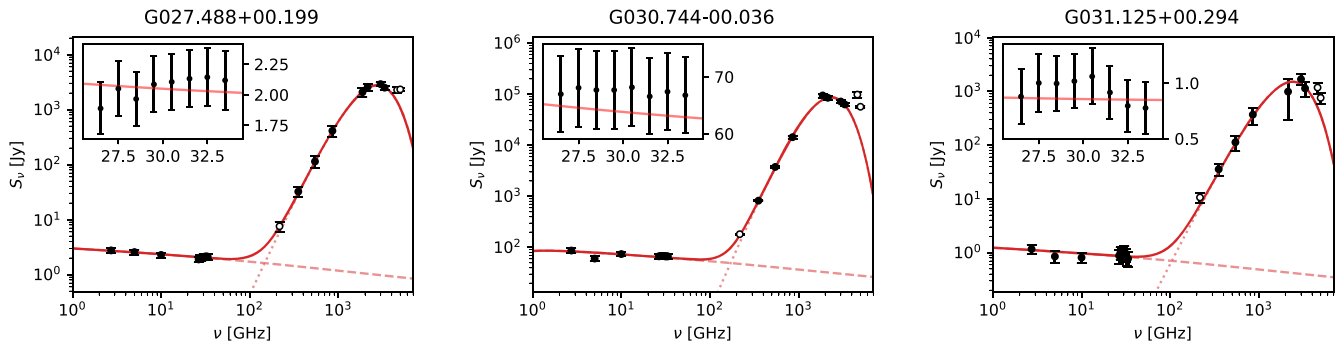
Figure 4. SEDs of three H II regions without an AME detection. Filled circles are used in the fit while open circles are not. The free–free and thermal dust components are shown as dashed and dotted lines, respectively. The total emission model is shown as a thick red line. The inset shown on the upper left of all plots shows the COMAP in-band 26–34 GHz spectrum.

this section we will discuss nine sources selected from the COMAP Galactic Plane Survey that are coincident with H II sources, six of which we find to have a $>3\sigma$ 30 GHz excess that is indicative of AME, and three of which show no evidence of AME.

In Figure 4 we show the best-fit SED models to the non-AME sources that are dominated by optically thin free–free emission at 30 GHz, and Figure 5 shows the model fits to the six sources that exhibit a significant excess at 30 GHz above the fitted free–free emission component.

In Table 4 we give the χ^2/dof of each region, as well as the relative contribution to the χ^2/dof for data between 2.7–10 GHz (χ^2_{lo}), 26–35 GHz (χ^2_{COMAP}), and 100–4000 GHz (χ^2_{hi}). For most regions we find $0.5 < \chi^2/\text{dof} < 1.5$. Estimates where the χ^2/dof is less than unity are due to background correlation uncertainties not being accounted for and to the correlation between the calibration of each survey. The assumption that the calibration uncertainties we give in Table 2 are uncorrelated, results in an overestimate of the uncertainty for some regions. The worst-fitting regions are G030.744−00.036 (the core of W43) and G029.038−00.636 (RCW 175) with $\chi^2/\text{dof} \sim 3$. For G030.744−00.036 the large χ^2/dof is driven by the low-frequency data; specifically the flux density measured at 5 GHz using the Parkes survey is underestimated relative to the two other low-frequency surveys. We suppose that this is due to issues with the calibration of the Parkes data in this region, likely due to significant sidelobe pickup from the nearby, bright diffuse emission that surrounds G030.744−00.036 (although further investigation would be required to prove this). The other region with a high χ^2/dof is G029.038−00.636; in this case we find that the issue is associated with just the Akari data. A comparison between the IRAS and Akari data does not reveal any clear morphological differences (e.g., no point sources have been subtracted from the reprocessed IRAS data in the region), suggesting a systematic calibration issue with the Akari data along this line of sight.

We estimate the emission measure (EM $\equiv \int n_e^2 \, dl$) of each source from the fitted amplitude of the free–free model described in Section 4. We find that the aperture-averaged EM of the sources in our sample is in the range 5000–20,000 pc cm^{-6}, which is typical of classical H II regions (Kurtz 2002). The exception is W43 itself, which has a higher EM of 400,000 pc cm^{-6}, comparable to previous estimates of the brightest (and densest) central source with EM = 720,000 pc cm^{-6} (Downes et al. 1980), and as expected given that it is a massive star formation region. As all of the sources are either

approximately the size of the COMAP beam or slightly extended we are not significantly underestimating the true EM of the sources due to beam dilution; however the value does represent an average over the measured aperture area.

We also fit models for thermal dust emission, which give dust temperatures (T_d in Equation (12)) in the range 23–30 K. These measurements agree with Anderson et al. (2012), who reported dust temperatures of 25.3 ± 2.4 K averaged across whole H ii regions. Notably these dust temperatures are higher than those reported by Planck Collaboration et al. (2016b; 19.4 $\pm$ 1.3 K), who mainly considered the high-latitude sky, where dust is known to be colder.

Besides fitting full SED models we fit for the spectral index of the emission measured within the COMAP frequency band (26–34 GHz). The in-band spectral indices are given in Table 3 (α_{26-34}). We find that there may be evidence that AME regions are more likely to have rising spectra within the COMAP band; this will become clearer in the future as we measure more AME and non-AME regions in the COMAP Galactic Plane Survey.

The peak frequencies of the candidate AME sources are given in Table 3. We find that our peak frequencies are higher than the 25–30 GHz range found previously (e.g., Planck Collaboration et al. 2016a, 2018), with a mean value of $\nu_{\text{AME}} \sim 40$ GHz. We test several different priors and find that changes in the peak frequency for different priors are all consistent within the uncertainties. The apparently higher than expected AME peak frequency must therefore be driven by the lack of data between 40 and 100 GHz, meaning we cannot constrain the downturn in the AME spectrum. Although the peak frequencies we measure are generally high, they are still consistent within 1σ with the expected AME peak frequency of ~ 30 GHz.

The AME widths that we measure are within $0.55 < w_{\text{AME}} < 0.85$, similar to the range of widths measured in the λ Orionis ring (Cepeda-Arroita et al. 2021). In general, we find that the AME width is not well constrained for these sources for the same reason we cannot easily constrain the peak frequency (i.e., no data between 40 and 100 GHz). However, we do notice that there tends to be a relationship between the width of the AME spectrum and the measured in-band spectral index, with steeper in-band spectra leading to narrower widths implying we do have some constraining power from the COMAP data alone. However, at present this is not a clear relationship; for example G027.27.266+00.165 has a steep in-band spectrum but also a wide w_{AME}, which is mostly driven by an excess of emission seen in the 10 GHz Nobeyama data.
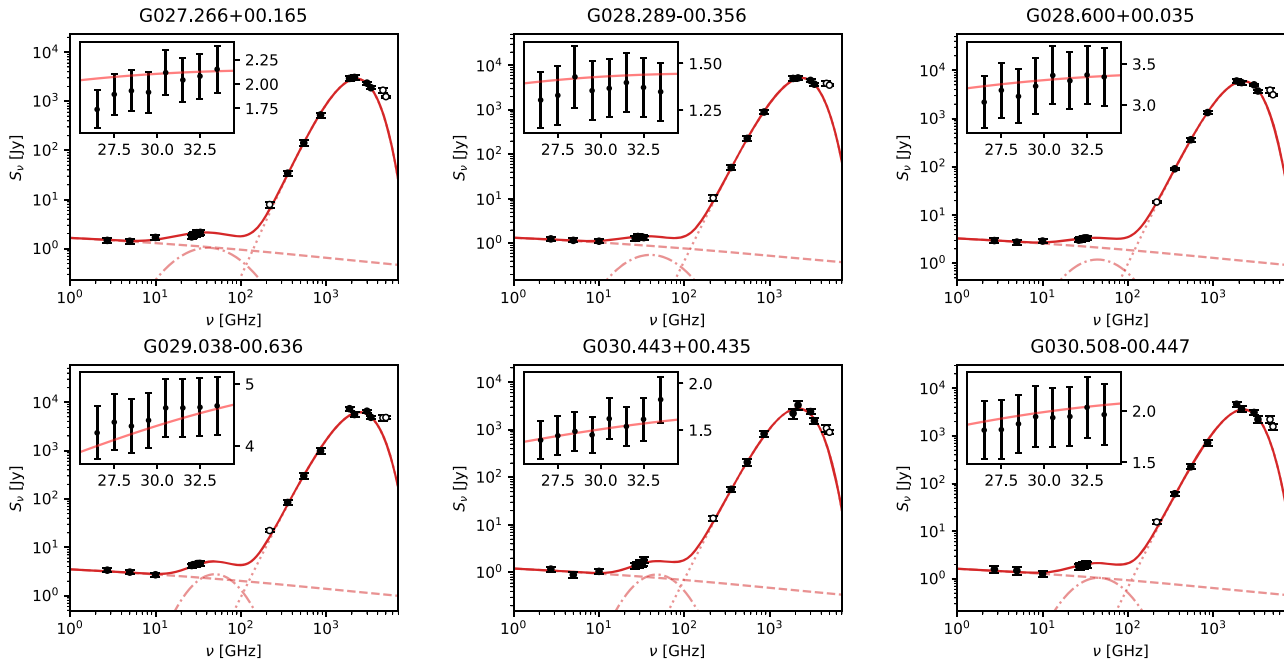
Figure 5. SEDs of six H II regions that show a significant AME detection. Filled circles are used in the fit while open circles are not. The free–free, spinning dust, and thermal dust components are shown as dashed, dashed–dotted, and dotted lines, respectively. The total emission model is shown as a thick red line. The inset shown on the upper left of all plots shows the COMAP in-band 26–34 GHz spectrum.

Table 4
Summary of Reduced χ^2/dof Values Determined for the Nine Sources in Table 3

Name	χ^2/dof	χ^2_{lo}	χ^2_{COMAP}	χ^2_{hi}
G027.266+00.165	1.53	0.18	0.97	0.39
G030.744−00.036	3.42	1.9	0.46	1.06
G031.125−00.294	1.01	0.34	0.38	0.29
G027.488+00.199	0.53	0.02	0.34	0.17
G028.289−00.356	0.55	0.04	0.34	0.17
G028.600+00.035	0.61	0.08	0.15	0.38
G029.038−00.636	2.99	0.59	0.08	2.33
G030.443+00.435	1.31	0.38	0.25	0.68
G030.508−00.447	1.52	0.11	0.11	1.3

Note. χ^2/dof values are given for the whole fitted data set alongside the contributions from data points with $\nu < 26$ GHz (χ^2_{lo}), for the eight COMAP bands (χ^2_{COMAP}), and for data sets with $\nu > 34$ GHz (χ^2_{hi}).

In order to obtain the AME emissivity (brightness per unit column density of dust) for each source (ϵ_ν) we use the excesses and τ_{353} values reported in Table 3. We convert τ_{353} to a column density via $(8.4 \pm 3.0) \times 10^{-27}$ cm^2 H^{-1} as reported by Planck Collaboration et al. (2014) for the whole sky. The uncertainties are dominated by this conversion factor. These values make up the last column in Table 3 and show a clear difference between non-AME sources (most of which are consistent with zero emissivity) and the AME regions, which typically have emissivities of the order of 10^{-17} at 30 GHz.

In Figure 4 we show the SEDs of the H II regions in which we find no evidence of AME. The SEDs are fitted with a two-component free–free plus thermal dust model. The region G027.488+00.199 is located near to the H II region G027.266 +0.165 and just outside of the ring structure marked in Figure 2. The H II region G031.125−00.294 lies near the exterior of the

larger W43 complex. Both G027.488+00.199 and G031.125 +00.294 are classical H II regions; they contain a number of infrared dark clouds (IRDCs; Peretto & Fuller 2009) but are not associated with any known stellar clusters or ionizing main-sequence stars (Reed 2003; Bica et al. 2019). The region G030.744−00.036 is centered on W43, one of the Galaxy's most active star formation regions (e.g., Nguyen Luong et al. 2011); using a central 8′ aperture we measure a flux density of ~100 Jy, approximately 20% of the flux density of the entire region (Irfan et al. 2015; Génova-Santos et al. 2017).

In the following we will discuss the properties of each extracted H II region in more detail. In Figure 6 we show the Spitzer 8 μm GLIMPSE (image; Churchwell et al. 2009; GLIMPSE Team 2020) and Herschel 250 μm Hi-GAL survey (contours; Molinari et al. 2016) data of each region in which we detect AME. All of these regions are sites of active or recent star formation. The annotations are the H II region designations defined in Anderson et al. (2014); we also mark the locations of bright 5 GHz sources from the CORNISH survey (Purcell et al. 2013), the locations of IRDCs (Peretto & Fuller 2009), and any known O/B stars (Reed 2003).

5.4.1. G027.266+00.165

The G027.266+00.165 region contains two H II regions at a distance of ~2.6 kpc (Anderson et al. 2014), and is coincident with a larger ring of diffuse emission (marked in Figure 2) that is visible at $\nu < 40$ GHz and in the far-infrared IRAS data. We can see in Figure 6 that the H II region G027.276+00.148 is centered in the aperture. The second H II region G027.334 +00.176 appears to exhibit a photodissociation region (PDR) along its lower boundary (identified by the arc of emission subtending $\approx 0°.1$ seen at 8 μm on the edge of the IRDC), which may be associated with the nearby embedded cluster (Bica et al. 2019); PDRs have previously been found to be sources of AME (Casassus et al. 2008).
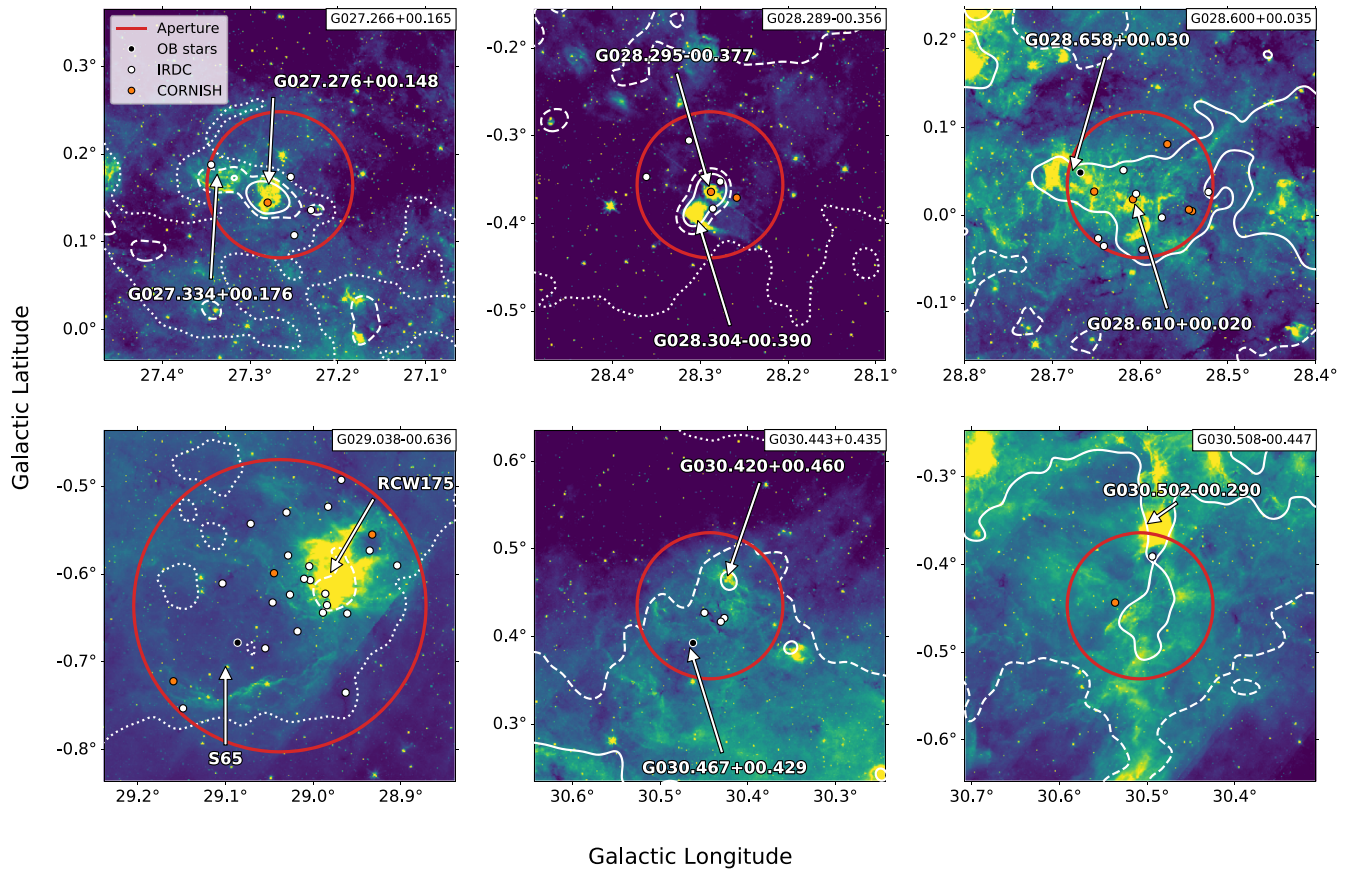
Figure 6. Spitzer 8 μm IRAC image (GLIMPSE Team 2020) of each H II region where we find significant AME. The contours are from the 250 μm Hi-GAL data at 1000 (*dotted* line), 2000 (*dashed* line), and 3000 MJy sr^{-1} (*solid* line). The *red circle* marks the aperture used to measure the SED. The *white* markers show the locations of the IRDCs from Peretto & Fuller (2009). Sources from the CORNISH survey $>7\sigma$ catalog are shown as *orange* markers (Purcell et al. 2013). *Black* markers indicate O/B stars (Reed 2003).

We find that the AME emissivity of this region is the highest out of all the AME detections (10.1 $\pm$ 3.8 Jy sr^{-1} cm^2 H^{-1}; Table 3), which could potentially be linked to the presence of the PDR. In 250 μm data we see that the cold dust emission is largely concentrated around the main central H II region and the nearby IRDCs. The very large dust columns associated with IRDCs could be associated with regions of high AME emissivity (e.g., Ysard et al. 2011), which is another possible explanation for the region's high emissivity. Finally, it is interesting that we do not detect any AME in the nearby H II region G027.488+00.199, despite their being physically close together and sharing similar environmental conditions. However, there is one key difference between the two regions: G027.266+00.165 is coincident with the diffuse background emission of the ring marked in Figure 2 while G027.488 +00.199 is separated from it, which suggests the AME may be associated with the diffuse background emission and not necessarily with the H II region itself.

The 10 GHz data point in Figure 5 is seen to rise above the free–free emission spectrum. One possible explanation for this rise is simply a systematic issue with 10 GHz data in this region. Another possibility is that it is evidence for an optically thick UCHII region with a turnover frequency of $\sim$10 GHz. In Section 5.3 we discuss the typical UCHII contributions at 30 GHz but there are a number that are much brighter than average, one of which happens to be within the G027.266 +00.165 region. To determine whether this specific UCHII region is optically thick at 30 GHz we use the deconvolved

source size (5″5) and integrated flux density ($S_5 = 0.428$ Jy) provided in the CORNISH catalog (Purcell et al. 2013), and calculate the brightness temperature at 5 GHz. We find that the brightness temperature of this UCHII region is $<$1000 K at 5 GHz, much less than the typical electron temperature of H II regions ($\sim$10^4 K), which implies that the region is optically thin at 5 GHz, and therefore cannot explain the excess we see at 30 GHz.

5.4.2. G028.289−00.356

This region contains two H II regions G028.295−00.377 and G028.304−00.390 at distances of 3.3 kpc and 4.8 kpc, respectively (Anderson et al. 2014). Both H II regions contain embedded clusters (Bica et al. 2019). The source is not resolved by the COMAP beam. Besides the two H II regions, the aperture contains three IRDCs, and two candidate UCHII sources identified by the CORNISH survey (Yang et al. 2021). This region does not have any clear evidence of large PDRs, or any known O/B stars. We estimate the two UCHII regions to be both optically thin at 5 GHz, and therefore to not contribute to the observed AME excess seen by COMAP.

5.4.3. G028.600+00.035

The region G028.600+00.035 lies close to the Galactic plane, and is embedded within a much larger complex that is clearly visible at 30 GHz in Figure 2. It contains the H II region G028.610+00.020 near the center of the aperture, and another

H II region G028.658+00.030 that is found near to the edge; both H II regions are at a distance of 6.2 kpc (Anderson et al. 2014). G028.658+00.030 contains the high-mass star LS IV -03 8 (Reed 2003). This region is potentially the most active star formation region of the six AME candidate sources, containing five UCHII candidates from the CORNISH survey, and six IRDCs (Peretto & Fuller 2009). The COMAP emission shows that this source is slightly extended (6′9; Table 3), and the peak in the 30 GHz emission is not coincident with either of the H II regions. There is a bright filamentary structure in the 8 μm data, which might be evidence of an extended PDR. This region is also the brightest AME region in the 250 μm data, implying it has the highest cold dust column density of all six AME regions.

Of the six UCHII regions five are extended, all with estimated mean surface brightness temperatures of $T_b^{\rm ff} < 1000$ K, implying they are optically thin and therefore are fitted by the optically thin free–free emission model. The one unresolved UCHII region in the CORNISH catalog has a flux density of 3.23 mJy and contributes a negligible flux density at 30 GHz even if it is optically thick.

5.4.4. G029.038−00.636

This region contains two H II regions: RCW 175 (Rodgers et al. 1960), and S65 (Sharpless 1959)—both regions have a kinematic distance of ∼3 kpc (Lee et al. 2012). The region has been studied several times before and is a well-known source of AME (Dickinson et al. 2009; Tibbs et al. 2012; Battistelli et al. 2015). RCW 175 is an extended source ≈10′ in size, and is clearly visible in the 8 μm data. The region contains an embedded cluster (Bica et al. 2019), a high density of IRDCs (14 in total; Peretto & Fuller 2009), and a large number of protostellar objects (Kuhn et al. 2021) making this object one of the more active star-forming regions in our sample.

The other H II region S65 (Sharpless 1959), which is associated with the O/B star ALS 19303 (Reed 2003), is not visible at 8 μm but is visible at radio frequencies (Paladini et al. 2003) indicating it is likely a Strömgren sphere (a spherical region of ionized gas surrounding a young O/B-type star; Strömgren 1939). We can see that there is a bubble of swept-up circumstellar material around the boundary of S65, and that there is evidence of a PDR visible at 8 μm along the lower edge of the region.

The region is resolved in the COMAP data, with a geometric mean diameter of 12′7. Interestingly we find that the peak in the COMAP 30 GHz map is not coincident with either H ii region but instead rises between the two—though it is not clearly coincident with any particular feature such as the PDR seen near S65.

There are two candidate UCHII regions within the CORNISH survey for RCW 175. One of these has a flux density of $S_5 = 4.65$ mJy, resulting in a negligible contribution at 30 GHz. The other has a flux density of $S_5 = 20.21$ mJy, which if we use the maximum turnover frequency of 16.7 GHz given in Section 5.3 gives an upper limit of $S_{30} = 0.2$ Jy at 30 GHz—much less than the observed 30 GHz excess ($\Delta S_{30} = 1.97 \pm 0.14$).

5.4.5. G030.443+0.435

This region is situated above the larger diffuse W43 complex as seen in Figure 2 and contains a single bright H II region:

S66/RCW 176 (Sharpless 1959; Rodgers et al. 1960), which is referenced as G030.420+00.460 in the Wide-field Infrared Survey Explorer (WISE) H II catalog at a distance of 3.6 kpc (Anderson et al. 2014) and potentially contains an embedded cluster (Bica et al. 2019). The WISE catalog cites a second H II region G030.467+00.429, which is not associated with any emission at 8 μm but is visible in the radio (Paladini et al. 2003); the region may be ionized by the coincident high-mass star LS IV -02 16 (Reed 2003). Unlike other AME regions discussed, there are no associated compact 5 GHz sources in the CORNISH catalog, implying there is no current high-mass star formation. Several IRDCs are found to be clustered around the center of the aperture, and to be coincident with the 30 GHz COMAP emission. These are likely the source of the AME and would be ideal candidates for high-frequency follow-up observations.

5.4.6. G030.508−00.447

G030.508−00.447 is situated below the W43 complex as seen in Figure 2. The region is dominated by a diffuse spur of emission that is correlated at all frequencies implying that the gas and dust within the ISM are highly mixed in this region. This is the only region in this sample that does not contain an H II region within the COMAP aperture. G030.502−00.290 lies just outside the aperture at a distance of 7.3 kpc, but it may not be directly associated with the dust spur. There is a single IRDC with a high peak 8 μm opacity of $\tau_{8\mu m} = 5.68$ (Peretto & Fuller 2009) near to the edge of the aperture, but it appears that most of the emission at 8 μm has at least some absorption, indicative of a high-density cloud. Although there is no compact H II source, the region is still undergoing active star formation with 15 candidate young stellar objects (most of which are early-stage protostellar objects: Class I/II) mostly concentrated around the IRDC although several are scattered throughout the spur (Kuhn et al. 2021).

We find that there is only one faint CORNISH source with a 5 GHz flux density of $S_5 = 6$ mJy, which we find to be optically thin and to make a negligible contribution to the observed COMAP 30 GHz emission.

5.5. SNRs

Few SNRs are readily detectable at higher radio frequencies ($\nu \gtrsim 30$ GHz), owing to their synchrotron spectra's typical behavior of steeply falling with frequency ($\alpha \sim -0.7$) and to increased background. However, the brightest SNRs and those with a flatter spectrum ($\alpha > -0.5$) are detectable. Those with flat radio spectra tend to have a filled-center or mixed morphology (rather than just a shell) and are often associated with a pulsar wind nebula (PWN); the Crab Nebula is one of the best examples (for a review, see Dubner & Giacani 2015).

A wide range of spectra have been observed, particularly over a wide frequency range, where a different population of electron energies are probed. The differences are thought to be due to the various intrinsic and extrinsic sources of energy injection/losses, resulting in a variety of spectra and morphologies (Urošević 2014; Dubner & Giacani 2015). Thus, high-frequency observations are useful for understanding energy losses/reacceleration as well as for characterizing nonsynchrotron components and distinguishing them from free–free emission and AME. Indeed, a number of SNRs have been reclassified as H II (e.g., Dokara et al. 2021).

Table 5
Summary of Measurements of Six SNRs Detected in the Current COMAP Survey

Name	θ (′)	S_{30} (Jy)	$\alpha_{2.7-30}$	α_{26-34}
G021.5−0.9	5	$5.52^{\pm0.56}$	$-0.07^{\pm0.06}$	$+0.14^{\pm0.09}$
G021.8−0.6 (Kes 69)	20	$5.99^{\pm0.69}$	$-0.77^{\pm0.06}$	$-1.30^{\pm0.30}$
G31.9+0.0 (3C 391)	7×5	$3.08^{\pm0.34}$	$-0.60^{\pm0.06}$	$-1.05^{\pm0.22}$
G34.7−0.4 (W44)	35×27	$41.0^{\pm4.2}$	$-0.54^{\pm0.06}$	$-0.50^{\pm0.11}$
G35.6−0.4	15×11	$6.2^{\pm1.1}$	$-0.34^{\pm0.08}$	$-2.5^{\pm0.5}$
G039.2−0.3 (3C 396)	8×6	$6.83^{\pm0.73}$	$-0.25^{\pm0.06}$	$+0.11^{\pm0.11}$

We have inspected the entire 30 GHz COMAP survey to date at the location of the 33 known SNRs from the most recent version[16] of the Green supernova catalog (Green 2019) over the longitude range $l = 20°–40°$. Most of these SNRs show no obvious source in the COMAP map, or are confused with other nearby sources and background emission. There are six SNR sources of interest, three of which are very extended ($\gtrsim 10'$) and three are compact or only slightly larger than the beamwidth ($\gtrsim 5'$). We also look at the positions of new SNR candidates from Dokara et al. (2021) but no obvious detection is possible.

We briefly discuss them in turn and include our flux density measurement at 30 GHz along with the spectral index from 2.7 GHz to 30 GHz and the in-band spectral index fitted separately over the 26–34 GHz COMAP frequency range. The results are given in Table 5. For each SNR, we adjust the aperture size to be suitable for the SNR and use a background annulus that is 1.3–1.6 times the radius. The SEDs of these six SNRs are presented in Figure 7, showing our measurements from the maps available to us as well as values from the literature. Note that in order to stay as consistent with the literature as possible, we use the name (and coordinate convention) first allocated to each of the six SNRs when referring to it.

5.5.1. G34.7−0.4 (W44)

We begin with W44 (G34.7−0.4, 3C 392), which is a well-studied SNR residing in and interacting with a giant molecular cloud (e.g., Rho et al. 1994) at a distance of ≈ 3 kpc. W44 is clearly visible in the COMAP 30 GHz map (Figure 1) and is similar in appearance in low-frequency radio maps (e.g., Castelletti et al. 2007). It has a distorted morphology over approximately $0°.5$ but with a clear shell across to the SE. Previous estimates of the radio spectral index are around $\alpha = -0.4$ to -0.3 between 0.02 and 1 GHz. However, recent observations by the Sardinia Radio Telescope (SRT) at 1.5 and 7 GHz (Egron et al. 2017) and at 21.4 GHz (Loru et al. 2019) have shown that the spectrum *steepens* dramatically at high ($\gtrsim 10$ GHz) frequencies, suggesting that there is a spectral break in the cosmic-ray energy spectrum, which has already been observed with gamma-ray observations of W44 (Ackermann et al. 2013).

Using the higher-frequency data from COMAP we can help confirm the energy of the spectral break, and help constrain the mechanism behind cosmic-ray production in W44. Given the complexity of the region and its large angular size (which allows spectral variations across the source to be assessed), we will present a detailed analysis in a future work (S. E. Harper

---

et al. 2022, in preparation). Nevertheless, our initial analysis finds a flux density of $S_{30} = 41.0 \pm 4.2$ Jy, which is consistent with a power-law model from lower frequencies (Figure 7). The best-fitting spectral index is $\alpha_{2.7-30} = -0.54 \pm 0.06$, with the in-band spectral index $\alpha_{26-34} = -0.50 \pm 11$. Therefore, the integrated SED appears to be well approximated by a power law over the range 1–30 GHz. We do not see evidence of the level of steepening observed by Loru et al. (2019), who measured spectral indices above 7 GHz of $\alpha \approx -1$. Loru et al. (2019) noted that their 21.4 GHz flux density of 25 ± 3 Jy falls far short of fits to lower-frequency data; our power-law fit predicts 49.1 ± 0.6 Jy at 21.4 GHz. However, low-frequency SRT data from Egron et al. (2017) are consistent with our power-law relation, with fluxes of 214 ± 6 and 94 ± 4 Jy at 1.5 and 7 GHz, respectively. Given the high angular resolution of the SRT data, and the large-scale negatives apparent in their map (see Figure 5 in Egron et al. 2017), it is possible that there could be some flux loss in the SRT data, which could be responsible for an underestimation of the integrated flux of W44 and steeper indices.

5.5.2. G021.5−0.9

G021.5−0.9 is a relatively compact ($<5'$) bright source associated with a PWN (Bietenholz et al. 2011). It is detected with a high S/N as a compact source in the COMAP maps. With a $5'$ aperture we find $S_{30} = 5.52 \pm 0.56$ Jy, which is consistent with the 32 GHz Effelsberg measurements of 5.64 ± 0.29 Jy (Morsi & Reich 1987). The radio spectrum has been measured to be close to flat ($\alpha = -0.06 \pm 0.03$) up to tens of gigahertz, which we confirm ($\alpha_{2.7-30} = -0.07 \pm 0.06$). The spectrum is known to have a spectral break around 30–40 GHz (Becker & Kundu 1976; Morsi & Reich 1987; Salter et al. 1989b; Bietenholz et al. 2011) with $\alpha = -0.37 \pm 0.19$ between 32 and 84 GHz (Salter et al. 1989b). Our in-band spectral index is also consistent with a flat spectrum ($\alpha_{26-34} = 0.14 \pm 0.09$) indicating that the spectral break must be above 34 GHz and must be relatively sharp. This is supported by the data at frequencies ~ 100 GHz (see Figure 7).

5.5.3. G021.8−0.6 (Kes 69)

G021.8−0.6 (Kes 69) is a diffuse and extended SNR $20'$ in size (e.g., Bietenholz et al. 2011). G021.8−0.6 has a limb-brightened shell, which is visible in the COMAP survey, while the rest of the shell is difficult to discern without background removal. Very few measurements have been made at higher radio frequencies (>10 GHz).

Figure 7 shows the SED with data from the literature and our own analysis. At lower frequencies, the spectrum is well fitted to a power law up to 10 GHz with $\alpha = -0.56 \pm 0.03$ (Sun et al. 2011). Unlike plerionic SNRs (Crab-like, driven by a central pulsar), this SNR is dominated by its shell. We do not attempt to measure the total flux density of the source as a whole, but instead focus on the limb-brightened shell using a $10'$ aperture. We find spectral indices of $\alpha_{2.7-30} = -0.77 \pm 0.06$ and $\alpha_{26-34} = -1.30 \pm 0.30$. Both of these values hint at some spectral aging above 10 GHz, increasing with frequency.

5.5.4. G31.9+0.0 (3C 391)

G31.9+0.0 (3C 391) is a well-known shell-dominated SNR of size $7' \times 5'$. It has a well-measured spectrum (Sun et al. 2011) that is flat below 1 GHz. Above 1 GHz, there is a spectral
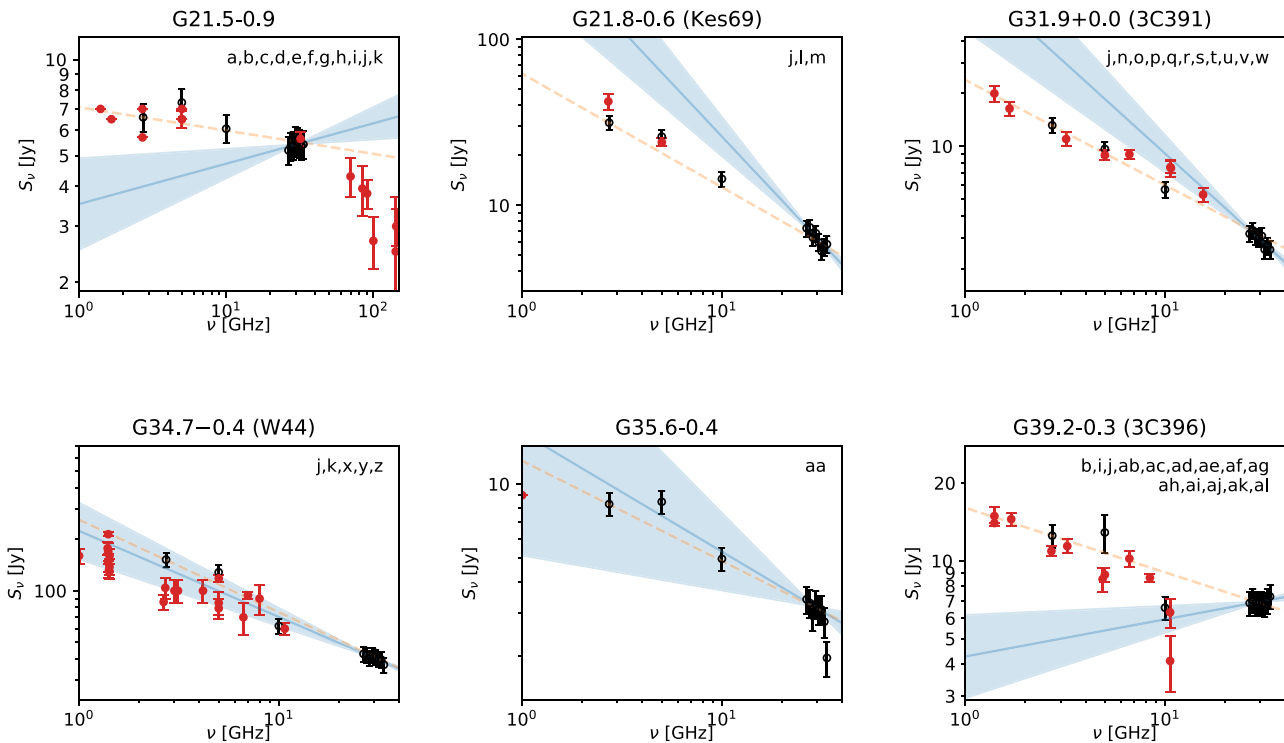
Figure 7. SEDs of the six SNRs discussed in Section 5.5 showing extracted flux densities in *black*, with literature values in *red* (the references for these points are given on the top right of each plot). Each SED also shows the fitted 2.7–30 GHz power-law model (*orange dashed* line) and the in-band 26–34 GHz fit (*blue* line). The in-band spectrum is extrapolated to lower/higher frequencies as a power law, with the *blue* shaded region showing the associated 1σ uncertainty. Note that for G35.6 −0.4 we show the fitted 26–32 GHz spectral index (i.e., without the last two COMAP bands) due to apparent evidence of a spectral break in the in-band spectrum. References: (a) Clark & Crawford (1974); (b) Altenhoff et al. (1979); (c) Milne & Hill (1969); (d) Goss & Day (1970); (e) Reifenstein et al. (1970); (f) Morsi & Reich (1987); (g) Salter et al. (1989b); (h) Salter et al. (1989a); (i) Kassim (1992); (j) Sun et al. (2011); (k) Planck Collaboration et al. (2016c); (l) Velusamy & Kundu (1974); (m) Green et al. (1997); (n) Dulk & Slee (1972); (o) Caswell et al. (1971); (p) Artyukh et al. (1969); (q) Condon (1971); (r) Kesteven (1968); (s) Pauliny-Toth & Kellermann (1966); (t) Bridle & Kesteven (1971); (u) Chaisson (1974); (v) Goss et al. (1979); (w) Moffett & Reynolds (1994); (x) Clark & Crawford (1974); (y) Castelletti et al. (2007); (z) Egron et al. (2017); (aa) Green (2009); (ab) Dickel & Denoyer (1975); (ac) Becker & Kundu (1976); (ad) Becker & Helfand (1987); (ae) Dulk & Slee (1975); (af) Shaver & Goss (1970); (ag) Kellermann et al. (1969); (ah) Reich et al. (1984); (ai) Downes et al. (1981); (aj) Day et al. (1970); (ak) Hughes & Butler (1969); (al) Cruciani et al. (2016).

break (Moffett & Reynolds 1994) into a power law–like spectrum with $\alpha = -0.54 \pm 0.02$ (Sun et al. 2011). Using a 7′ aperture we find $S_{30} = 3.08 \pm 0.34$ Jy and $\alpha_{2.7-30} = -0.60 \pm 0.06$. The in-band spectrum is $\alpha_{26-34} = -1.05 \pm 0.22$. These are both consistent with previous fits, but with an indication of steepening above 30 GHz. As noted by Sun et al. (2011), the spectrum appears to be slightly more complicated than a simple power law; there are hints that the spectrum flattens around 10 GHz and then steepens again above 30 GHz in the literature (see Figure 7). However, our best-fitting power law to our own extractions is consistent with a power law from 2.7 GHz to 30 GHz, with only a hint of steepening above 30 GHz.

A broken power-law trend would be typical of an aging SNR, where high-frequency photons begin to suffer energy loss through radiative cooling. This causes the spectral index to steepen for frequencies greater than the break frequency (typically around a few tens of gigahertz). As this happens, a morphological change occurs, from a shell and toward a composite shape, which may be identified by higher-resolution instruments such as the VLA.

5.5.5. G35.6−0.4

G35.6−0.4 is an interesting source that was initially classified as an SNR but was then removed following its identification as a thermal source, possibly due to the nearby planetary nebula IRAS 18554+0203. Using new radio data

Green (2009) reidentified the source as an SNR. It is an extended source of 15′ × 11′ with a limb-brightened shell. Very few measurements exist for this source (Figure 7). Green (2009) measured a radio spectral index of $\alpha = -0.47 \pm 0.07$. It is detected at a high S/N at 2.7 GHz but is weak at 30 GHz, barely being detected in the COMAP map. Nevertheless, we use a 15′ aperture to estimate the spectral index and find $\alpha_{2.7-30} = -0.34 \pm 0.08$, which is consistent with Green (2009), and supports the SNR nature of the source.

At higher frequencies we find that the in-band spectrum appears to be remarkably steep: $\alpha_{26-34} = -2.5 \pm 0.5$. However, the bright relative background makes this measurement difficult—hence the large uncertainty. We try varying the aperture/background annulus sizes and find this trend to be robust. We also notice some additional faint diffuse 30 GHz emission to the south of the SNR, which looks like interlocking shells, also visible in the 2.7 GHz data. This has not been observed before and possibly could be related to the SNR. An initial analysis with photometry does not yield a robust spectral index to confirm this, but it will be investigated in a future work.

5.5.6. G39.2−0.3 (3C 396)

Finally, G39.2−0.3 (3C 396) is a relatively well-known compact 8′ × 6′ SNR. A review of flux densities is given by Cruciani et al. (2016). At 33 GHz they give an updated VSA

flux density of 5.20 ± 0.33 Jy; however, this is after taking into account spatial filtering of the original measurement. Figure 7 indicates that some measurements, particularly at higher frequencies, are lower than expected compared to a simple power-law model.

With a $10'$ aperture we find $S_{30} = 6.83 \pm 0.73$ Jy, which is more consistent with the original 33 GHz value from the VSA (Scaife et al. 2007) of (6.64 ± 0.3) Jy. We find a best-fitting power law from 2.7 GHz of $\alpha_{2.7-30} = -0.25 \pm 0.06$, which is slightly flatter than previous fits at lower frequencies of $\alpha = -0.466 \pm 0.024$ over 150 MHz up to tens of gigahertz (Cruciani et al. 2016). This suggests that the spectrum may be flattening, possibly due to associated free–free or AME components, as originally suggested by Scaife et al. (2007). Our in-band value ($\alpha_{26-34} = 0.11 \pm 0.11$) is consistent with a flat spectrum, which supports this hypothesis. Such an additional component may originate in the region affected by the SNR, or it could be a thermal source along the line of sight.

5.6. RRLs

The ionized gas within H II regions and the surrounding diffuse interstellar gas (DIG) within the warm ionized medium (WIM) not only emit continuum free–free emission but also, when the gas is optically thin, can be observed via RRLs (Kardashev 1959). Besides being an alternative probe of the WIM, RRLs provide additional velocity information, and can be used to study the physics of the ISM, such as electron temperatures, abundances, ionization fractions, and non-LTE effects (Brown et al. 1978). For the study of AME at 30 GHz, RRLs are useful because they have a direct relationship with the continuum free–free emission (Rohlfs et al. 2013; Alves et al. 2015) in both discrete H II regions (e.g., Paladini et al. 2003; Bania et al. 2010; Anderson et al. 2011) and the DIG (Luisi et al. 2020; Anderson et al. 2021) from the leakage of Lyα photons from nearby H II regions (e.g., Zurita et al. 2000).

In addition to measuring continuum emission from the Galactic plane, COMAP can map emission lines within $26 < \nu < 34$ GHz. In this first analysis we will discuss the five hydrogen RRLs within the COMAP band: H(62)α to H(58)α. The COMAP spectrometer velocity resolution is $\sim$20 km s^{-1}, just wide enough to resolve these RRLs, which have a typical $\Delta V_{\frac{1}{2}} \sim 25$ km s^{-1}. We will focus our attention on the bright region W43, where RRLs have been extensively studied before (e.g., Hoglund & Mezger 1965; Alves et al. 2015; Luisi et al. 2020).

To process the RRLs we select chunks of spectra within ± 200 km s^{-1} around the rest frequencies of the five available RRLs. Then for each observation we fit a first-order polynomial across the spectrum, excluding the velocity range (in the local standard of rest, V_{LSR}) known to contain W43: $0 < V_{LSR} < 175$ km s^{-1}. To map the spectra we use a simple weighted-averaging map-making method since, unlike with the continuum data, we can assume the data are dominated by white instrumental noise. The calibration, observations, and other data processing are the same as described in Section 2.2.

In Figure 8 we show a map centered on W43 of the integrated RRLs after stacking all five lines; the contours are of the COMAP 26.5 GHz continuum data. The map has units of K km s^{-1} and a resolution of $4'.5$. We can clearly see in the center of the map the W43 complex, but we also see the bright H II region and molecular cloud complex G29.93−0.03, also known as W43-South. Between the W43 and W43-South
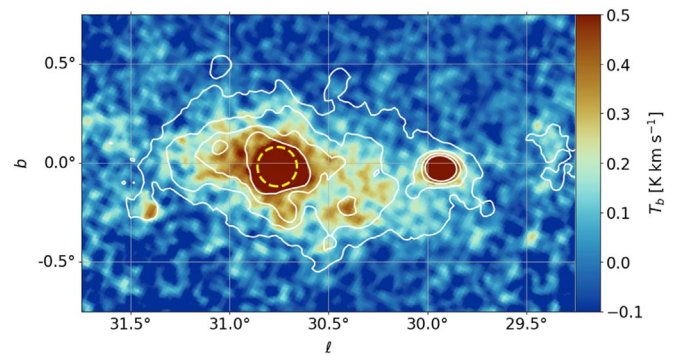
Figure 8. Map of the total RRL-integrated emission in units of K km s^{-1} after stacking all five RRLs in velocity. The contours correspond to the measured continuum emission at 26.5 GHz. The *dashed yellow* circle indicates the area used to measure the lines shown in Figure 9.

complexes we can see RRL emission originating in the DIG, which can be seen to be strongly correlated with the continuum emission shown by the contours. Detection of RRLs in the DIG at a similar resolution to that of COMAP has also recently been made at 4–8 GHz (Luisi et al. 2020; Anderson et al. 2021).

Figure 9 shows the individual lines measured along the line of sight toward W43 (marked by the *dashed yellow* circle in Figure 8). We make clear detections of the H(58)α–(62)α lines but we also see evidence of the He transition, which is offset from the main H transition line by -122.166 km s^{-1}. The final panel of Figure 9 shows the average of all five lines. The fitted peak velocity of the region is found to be $V = 90.9$ km s^{-1}, which agrees with other RRL surveys of W43 (97.5 ± 0.6 km s^{-1}; Alves et al. 2012).

It is possible to estimate the electron temperature (T_e) using the known relationship of the ratio between the integrated line brightness and the underlying continuum emission:

$$\frac{\int T_L dV_{km\,s^{-1}}}{T_C} = 1.0534 \times 10^4 \frac{T_e^{-1} \nu_{GHz}^1}{g_{ff}(\nu, T_e)}, \quad (18)$$

where $\int T_L dV$ is the integrated line emission, T_C is the continuum emission brightness, ν is the frequency, and $g_{ff}(\nu, T_e)$ is the Gaunt factor given by Equation (11).

In Table 6 we report the measured line velocities, the line-to-continuum ratios, and the derived electron temperatures using Equation (18) for each RRL measured toward W43. We find that the derived electron temperatures are much higher than those previously reported; for example in Alves et al. (2012) the electron temperature of W43 was found to be $T_e = 5660 \pm 190$ K. The reason for this discrepancy is that we do not attempt to correct for contributions to the continuum emission from sources other than free–free emission; hence we are overestimating the continuum emission since there will be some contribution from AME and to a lesser extent from synchrotron emission. An overestimate of the continuum brightness then leads to an overestimate of the electron temperature.

As discussed in earlier sections the two main emission components around 30 GHz will be either free–free emission or AME. By leveraging our knowledge of the electron temperature of W43 from Alves et al. (2012) we can estimate what fraction of the total emission is due to AME. The fractional
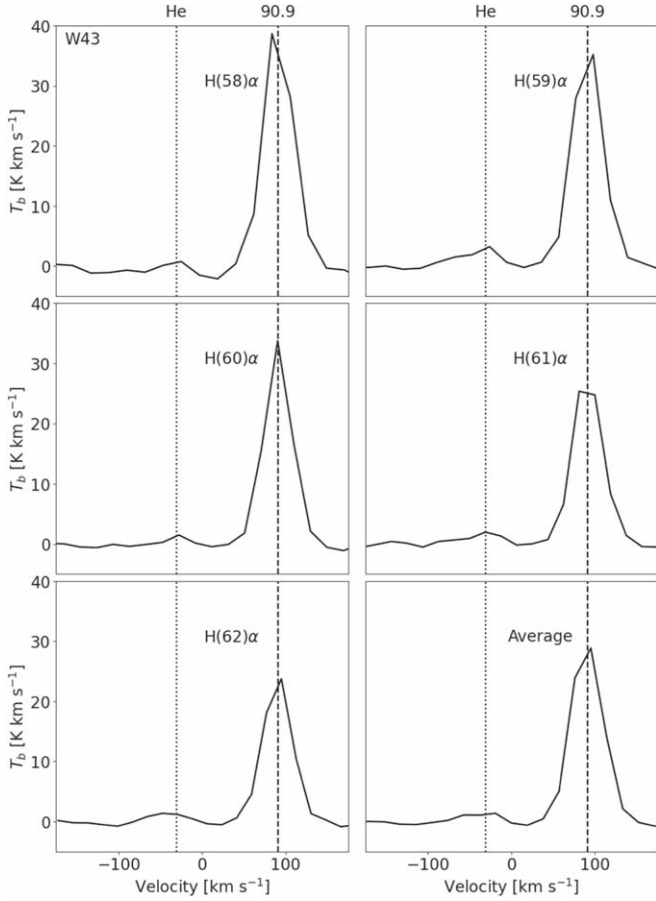
Figure 9. RRL spectra for the region indicated in Figure 8 centered on W43. We show each of the five RRLs in the COMAP 26–34 GHz band at a resolution of ~20 km s^{-1}. The final panel shows the average of all five lines binned into velocity bins of 20 km s^{-1}. The *dashed black* line marks the mean peak velocity of the five RRLs. We mark the nearby helium RRL with a *dotted black* line.

Table 6
RRL Properties of the W43 Region (Figure 8)

Line	V (km s^{-1})	$\frac{T_L dV}{T_C}$ (km s^{-1})	T_e (K)
H(62)α	90.9 ± 0.2	8.53 ± 0.15	7810 ± 120
H(61)α	91.2 ± 0.1	8.67 ± 0.10	8060 ± 80
H(60)α	90.8 ± 0.1	9.14 ± 0.09	8080 ± 70
H(59)α	91.1 ± 0.2	10.04 ± 0.09	7840 ± 60
H(58)α	90.4 ± 0.1	9.70 ± 0.07	8460 ± 50

Note. The electron temperature (T_e) is calculated using Equation (18). V is the fitted peak frequency of the RRL transitions, and $\frac{T_L dV}{T_C}$ is the line-to-continuum brightness ratio.

AME, for a given RRL, can be defined as

$$\eta_{\mathrm{AME}}^{\mathrm{RRL}} = \frac{T_{\mathrm{AME}}}{T_{\mathrm{ff}} + T_{\mathrm{AME}}} = 1 - \frac{\hat{a}_n}{a_n} = 1 - \frac{T_{\mathrm{ff}}}{T_{\mathrm{ff}} + T_{\mathrm{AME}}}, \quad (19)$$

where $\hat{a}_n$ is the line-to-continuum ratio we measure in Table 6 for transition H(n)α, a_n is the expected ratio given by Equation (18) and an assumed $T_e = 5660$ K, T_{AME} is the continuum brightness of the AME, and T_{ff} is the continuum brightness of the free–free emission. We find that the mean fractional AME within W43 at 30 GHz is $\eta_{\mathrm{AME}}^{\mathrm{RRL}} = 0.35 \pm 0.01$,

i.e., $(35 \pm 1)\%$, which is consistent with previous estimates (e.g., $37\% \pm 5\%$; Irfan et al. 2015).

These initial results show that the COMAP survey can readily detect RRLs from the Galaxy. The sensitivity is sufficient to detect several RRLs not only from the brightest H II regions but also from weaker sources including the DIG from multiple sightlines. Although not a dedicated survey with high velocity resolution, this will be a useful data set for the community.

6. Discussion and Conclusions

We have presented the first large-scale continuum/spectral survey at 30 GHz with an angular resolution significantly better than that of WMAP and Planck at the same frequencies. The COMAP instrument, being a focal plane array with a sensitive wideband receiver, is ideal for such a survey, which will eventually cover the Galactic plane at decl. $\gtrsim -10°$, which covers $\ell \approx 20°$–$220°$. We will also extend the latitude range for some longitudes where necessary, such as for the W40 region at $b \approx +3°.5$.

In this first paper, we have shown that there is a sufficient S/N to measure a large number of compact sources as well as diffuse emission. Furthermore, we can reliably extract several RRLs, which will provide a unique survey in itself. The calibration is good to at least $\approx5\%$ and potentially to $\approx1\%$ in the future.

On large scales $\gtrsim30'$, there remain some issues to be resolved. First, the existence of beam sidelobes means that the effective calibration can change by $\approx10\%$ as a function of scale. This can be corrected via deconvolution of the theoretical beam, although, in practice, this can be difficult due to missing pixels and inaccurate knowledge of the beam sidelobes. Similarly, on scales $\gtrsim1°$, filtering of the time-ordered data to reduce atmospheric and instrumental $1/f$ on scales of $\approx1°$ has caused a small loss of flux; our comparison of the integrated W43 flux density over a $2°$ diameter aperture to those of WMAP/Planck indicates a loss of $\approx15\%$–20%. This filtering is also why large-scale modes away from the bright Galactic plane in Figure 1 are not well constrained. This will be addressed and quantified using detailed simulations and comparisons with WMAP/Planck, in future work. Our hope is that by tuning the data analysis pipeline we can reduce these effects. Alternatively, we can combine the COMAP data on scales $\lesssim30'$ and the WMAP/Planck data on scales $\gtrsim30'$ to improve accuracy on all scales down to $5'$.

In this initial work, we have shown that a wide range of science can be investigated. The 30 GHz map is, on the whole, dominated by optically thin free–free continuum emission, with contributions from synchrotron emission along some lines of sight due to SNRs. We also find that there is evidence for a significant contribution of AME at 30 GHz, from the diffuse ISM at a level of $\eta_{\mathrm{AME}}^{\mathrm{diffuse}} = (22 \pm 2)\%$ of the total. For the individual regions we find the average percentage of AME at 30 GHz is $\langle\eta_{\mathrm{AME}}^{\mathrm{HII}}\rangle = (43 \pm 3)\%$. We emphasize that this value is likely biased high (compared to all H II regions) since we have chosen regions with AME and it is not a complete sample. Nevertheless, it is comparable to what has been found in some other H II regions (Todorovic et al. 2010; Planck Collaboration et al. 2018).

In Section 5.6 we find that RRLs underpredict the observed 30 GHz continuum emission within the core of W43; this excess we have interpreted to be due to AME with $\eta_{\mathrm{AME}}^{\mathrm{RRL}} = (35 \pm 1)\%$. Interestingly in Section 5.4 we find no

evidence of AME from the central core of W43, apparently contradicting the AME estimated by the RRLs, but this is because the RRL estimate also includes the contribution from the large-scale diffuse background behind the core of W43—implying the AME is associated more closely with the diffuse ISM than with the central W43 complex in this region.

Of the nine H II regions discussed in Section 5.4 we presented six that we find to contain AME and three that do not contain AME. As discussed above, the H II regions that we find to contain AME are probably special cases, as the diffuse emission and RRLs suggest AME is everywhere at 30 GHz. The environments of the six AME regions are diverse. PDRs have been suggested to be associated with AME (Casassus et al. 2008; Arce-Tord et al. 2020) and we see evidence for PDRs in four of the regions—G027.266+00.165, G028.658 +00.030, G029.038−00.636, and G030.443+0.435—but we do not see a PDR within one of our most significant AME detections (G030.508−00.447). Another possibility is the density of dust within the region, because dark clouds have been found previously to be progenitor sources for AME (e.g., Dickinson et al. 2010; Vidal et al. 2011; Harper et al. 2015), but again we find that IRDCs are prominent within each region and there is no correlation with the average or maximum IRDC optical depth. Using the data from the CORNISH survey we do find that each of the AME regions contains at least one UCHII region, while two of the non-AME regions contain none. However, we have shown that, in general, these UCHII regions are not significant contributors to the observed emission at 30 GHz. The presence of UCHII regions is a tracer of high-mass star formation (e.g., Habing & Israel 1979) indicating the AME regions may have stronger local interstellar radiation fields (ISRFs); this is thought to have an indirect impact on AME emissivity. Indeed, numerous studies have found a correlation between AME emissivity and ISRF strength (e.g., Tibbs et al. 2012; Planck Collaboration et al. 2018).

Modified blackbody fits to Planck HFI data (217–857 GHz) suggest that the Rayleigh–Jeans (R-J) tail of thermal emission is not significant at 30 GHz for these regions. Nevertheless, it will be interesting to search for the densest infrared dark dust clouds (e.g., Pari & Hora 2020) in the outer Galaxy (where diffuse free–free emission will be much weaker) that have yet to ionize their surroundings, where thermal dust may be detectable with the COMAP data. This would allow a test of the emissivity power-law model for thermal dust to much lower frequencies. These IRDCs may also be strong AME emitters (Scaife et al. 2010; Ysard et al. 2011; Tibbs et al. 2015).

In Figure 10 we show the AME emissivity at 30 GHz for each of the nine H II regions compared with predictions from SpDust (Ali-Haïmoud et al. 2009; Silsbee et al. 2011) for six different environments using the parameters given in Draine & Lazarian (1998). The weighted-average emissivity of the six AME regions is $(3.7 \pm 0.1) \times 10^{-17}$ Jy sr^{-1} cm^2 H^{-1} and is marked in the figure with a *black dashed* line. The uncertainties on the emissivities are driven by the uncertainty in the conversion of dust optical depth to column density as discussed in Section 5.4. We find that the six AME detections have emissivities that are of the magnitude expected from the models. We note that the model emissivities should not be overly interpreted since the environmental parameters are only rough guides and could change by a factor of several within the same phase of the ISM. It is not clear why there are two groups of AME emissivities. We do find that in the less
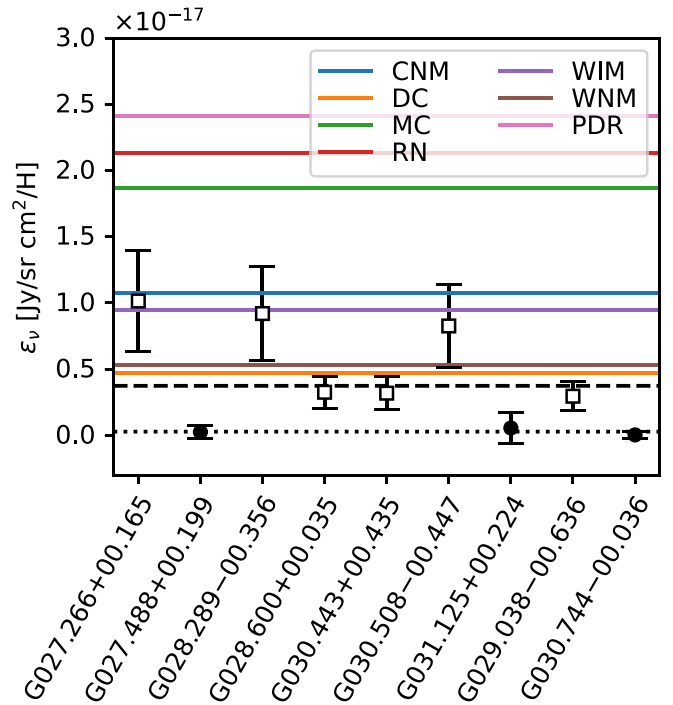
Figure 10. Plot of emissivities (calculated using the source sizes in Table 3) of all highlighted sources on the Galactic plane at 30 GHz across the different regions. The colored solid lines represent spinning dust models for a range of typical interstellar environments: cold neutral medium (CNM), dark clouds (DC), molecular clouds (MC), reflection nebulae (RN), WIM, warm neutral medium (WNM), and PDR. Sources categorized as AME or non-AME regions are plotted as white squares or filled circles, respectively. The weighted-average values are shown for the AME (dashed line) and non-AME (dotted line) regions.

emissive regions there is a nearby ionizing O/B star or association (Reed 2003); indeed, stronger ISRFs may destroy AME carriers (Dong & Draine 2011).

We detect six of the 33 known SNRs within the current survey region. As one would expect at this higher radio frequency, we are more sensitive to flat spectra ($\alpha > -0.5$) than to the majority of SNRs ($\alpha \lesssim -0.5$). These detections are typically filled-center SNRs or composite SNRs (filled center and a shell). These are often classed as "plerionic," containing emission from the central region as well as shells from shock waves. Typically, they host a pulsar and are referred to as PWNs, similar to the Crab Nebula (Tau A). Two of the six have $\alpha \approx -0.3$ from 2.7 to 30 GHz while G021.5−0.9 remains remarkably flat ($\alpha \approx 0$) to 30 GHz. Two of the six have steeper spectral indices ($\alpha \approx -0.7$). At the COMAP frequencies, we show evidence for steeper spectral indices indicative of spectral aging for two sources, while for W44 we find it is consistent with extrapolations from lower frequencies, in contradiction to the recent results of Loru et al. (2019). Of the 294 SNRs that are known (Green 2009) 79% are classified as shell SNRs, and $\approx 20\%$ as filled or composite, which are more likely to be flat-spectrum. Extrapolating based on these statistics and the number and level of COMAP detections made thus far, we expect to detect ~ 50 SNRs in the complete survey.

The spectroscopic nature of the COMAP data has also allowed us to extract five hydrogen RRLs with a spectral resolution of 20 km s^{-1}. Although the COMAP instrument was not designed for Galactic spectroscopic science (ideally we

would have much higher spectral/velocity resolution), we have shown that RRLs can be reliably extracted. The COMAP RRL survey represents the highest-frequency Galactic RRL survey to date. A comparison with the lower-frequency GDIGS 4–8 GHz RRL survey (Anderson et al. 2021) and HIPASS 1.4 GHz RRL survey (Alves et al. 2015) will be interesting, particularly for quantifying non-LTE effects. Even though they are very weak, we can map in RRLs not only the bright H II regions (which are brightest in free–free emission) but also diffuse emission away from H II regions down to a level of ≈ 0.1 K km s^{-1}. RRL data can be used to estimate electron temperatures or, if they are known, can be used to estimate the free–free continuum. Applying this to W43, we found that the continuum is $\approx 35\%$ brighter than expected, which we interpret as AME. The RRL data will be particularly useful for subtracting a model of free–free emission from the continuum map in order to investigate non-free–free components such as SNRs, AME, and the R-J tail of thermal dust.

Additional data will be important both for improving the SEDs and for understanding the nature of the ISM. At higher longitudes ($\ell \gtrsim 60°$) we will be able to include additional radio data from the 1.4 GHz Canadian Galactic Plane Survey (Landecker et al. 2010) and the AMI 15 GHz survey (Perrott et al. 2015). One limitation is the lack of data at frequencies ~ 40–100 GHz, which would significantly help in measuring the spectral shape of the AME (the peak frequency and width). This may be possible in the future with Atacama Large Millimeter/submillimeter Array bands 1–3 covering ≈ 35–116 GHz, using both the total-power and interferometric modes.

The COMAP 26–34 GHz survey is currently ongoing and is expected to be completed by 2023/24, covering the majority of the northern Galactic plane. The data, both continuum and RRL maps, will be released to the community when it is completed. In the meantime, we will be using the data to study the types of sources discussed in this paper in more detail. For example, when we have a large number of AME detections, we will be able to investigate the environments to understand what is driving the spinning dust.

ORCID iDs

Thomas J. Rennie https://orcid.org/0000-0002-1667-3897
Stuart E. Harper https://orcid.org/0000-0001-7911-5553
Clive Dickinson https://orcid.org/0000-0002-0045-442X
Liju Philip https://orcid.org/0000-0001-7612-2379
Kieran A. Cleary https://orcid.org/0000-0002-8214-8265
Richard J. Bond https://orcid.org/0000-0003-2358-9949
Patrick C. Breysse https://orcid.org/0000-0001-8382-5275
Roke Cepeda-Arroita https://orcid.org/0000-0002-9043-2645
Dongwoo T. Chung https://orcid.org/0000-0003-2618-6504
Delaney A. Dunne https://orcid.org/0000-0002-5223-8315
Hans Kristian Eriksen https://orcid.org/0000-0003-2332-5281
Marie Kristine Foss https://orcid.org/0000-0001-8896-3159
Andrew I. Harris https://orcid.org/0000-0001-6159-9174
Brandon Hensley https://orcid.org/0000-0001-7449-4638
Håvard T. Ihle https://orcid.org/0000-0003-3420-7766
James W. Lamb https://orcid.org/0000-0002-5959-1285
Roberta Paladini https://orcid.org/0000-0002-5158-243X
Timothy J. Pearson https://orcid.org/0000-0001-5213-6231
Anthony C. S. Readhead https://orcid.org/0000-0001-9152-961X
Nils-Ole Stutzer https://orcid.org/0000-0001-5301-1377
Duncan J. Watts https://orcid.org/0000-0002-5437-6121
Ingunn Kathrine Wehus https://orcid.org/0000-0003-3821-7275

References

Ackermann, M., Ajello, M., Allafort, A., et al. 2013, Sci, 339, 807
Ali-Haïmoud, Y., Hirata, C. M., & Dickinson, C. 2009, MNRAS, 395, 1055
Altenhoff, W. J., Downes, D., Pauls, T., & Schraml, J. 1979, A&AS, 35, 23
Alves, M. I. R., Calabretta, M., Davies, R. D., et al. 2015, MNRAS, 450, 2025
Alves, M. I. R., Davies, R. D., Dickinson, C., et al. 2012, MNRAS, 422, 2429
Anderson, L. D., Bania, T. M., Balser, D. S., et al. 2014, ApJS, 212, 1
Anderson, L. D., Bania, T. M., Balser, D. S., & Rood, R. T. 2011, ApJS, 194, 32
Anderson, L. D., Luisi, M., Liu, B., et al. 2021, ApJS, 254, 28
Anderson, L. D., Zavagno, A., Deharveng, L., et al. 2012, A&A, 542, A10
Arce-Tord, C., Vidal, M., Casassus, S., et al. 2020, MNRAS, 495, 3482
Artyukh, V. S., Dagkesamanskii, V. V., Vitkevich, R. D., & Kozhukhov, V. N. 1969, SvA, 12, 567

Bania, T. M., Anderson, L. D., Balser, D. S., & Rood, R. T. 2010, ApJL, 718, L106

Barbary, K. 2016, JOSS, 1, 58

Battistelli, E. S., Carretti, E., Cruciani, A., et al. 2015, ApJ, 801, 111

Becker, R. H., & Helfand, D. J. 1987, AJ, 94, 1629

Becker, R. H., & Kundu, M. R. 1976, ApJ, 204, 427

Bennett, C. L., Larson, D., Weiland, J. L., et al. 2013, ApJS, 208, 20

Bertin, E., & Arnouts, S. 1996, A&AS, 117, 393

Bica, E., Pavani, D. B., Bonatto, C. J., & Lima, E. F. 2019, AJ, 157, 12

Bietenholz, M. F., Matheson, H., Safi-Harb, S., Brogan, C., & Bartel, N. 2011, MNRAS, 412, 1221

Bonaldi, A., Ricciardi, S., Leach, S., et al. 2007, MNRAS, 382, 1791

Bridle, A. H., & Kesteven, M. J. L. 1971, AJ, 76, 958

Brown, R. L., Lockman, F. J., & Knapp, G. R. 1978, ARA&A, 16, 445

Brunthaler, A., Menten, K. M., Dzib, S. A., et al. 2021, A&A, 651, A85

Calabretta, M. R., Staveley-Smith, L., & Barnes, D. G. 2014, PASA, 31, e007

Carretti, E., Haverkorn, M., Staveley-Smith, L., et al. 2019, MNRAS, 489, 2330

Casassus, S., Dickinson, C., Cleary, K., et al. 2008, MNRAS, 391, 1075

Castelletti, G., Dubner, G., Brogan, C., & Kassim, N. E. 2007, A&A, 471, 537

Caswell, J. L., Dulk, G. A., Goss, W. M., Radhakrishnan, V., & Green, A. J. 1971, A&A, 12, 271

Cepeda-Arroita, R., Harper, S., Dickinson, C., et al. 2021, MNRAS, 503, 2927

Chaisson, E. J. 1974, ApJ, 189, 69

Churchwell, E. 2002, ARA&A, 40, 27

Churchwell, E., Babler, B. L., Meade, M. R., et al. 2009, PASP, 121, 213

Clark, D. H., & Crawford, D. F. 1974, AuJPh, 27, 713

Cleary, K. A., Borowska, J., Breysse, P. C., et al. 2022, ApJ, 933, 182

Collette, A., Kluyver, T., Caswell, T. A., et al. 2021, h5py/h5py: 3.5.0, v3.5.0, Zenodo, doi:10.5281/zenodo.5585380

Compiegne, M., Verstraete, L., Jones, A., et al. 2011, A&A, 525, A103

Condon, J. J. 1971, Cornell-Sydney Univ. Astronomy Centre Report, 238

Crameri, F. 2018, GMD, 11, 2541

Crameri, F., Shephard, G. E., & Heron, P. J. 2020, NatCo, 11, 5444

Cruciani, A., Battistelli, E. S., Carretti, E., et al. 2016, MNRAS, 459, 4224

Davies, R. D., Dickinson, C., Banday, A. J., et al. 2006, MNRAS, 370, 1125

Davies, R. D., Watson, R. A., & Gutierrez, C. M. 1996, MNRAS, 278, 925

Day, G. A., Warne, W. G., & Cooke, D. J. 1970, AuJPA, 13, 11

Delabrouille, J. 1998, A&AS, 127, 555

Désert, F. X., Macías-Pérez, J. F., Mayet, F., et al. 2008, A&A, 481, 411

Dickel, J. R., & Denoyer, L. K. 1975, AJ, 80, 437

Dickinson, C. 2018, Galax, 6, 56

Dickinson, C., Ali-Haïmoud, Y., Barr, A., et al. 2018, NewAR, 80, 1

Dickinson, C., Casassus, S., Davies, R. D., et al. 2010, MNRAS, 407, 2223

Dickinson, C., Davies, R. D., Allison, J. R., et al. 2009, ApJ, 690, 1585

Dickinson, C., Davies, R. D., Bronfman, L., et al. 2007, MNRAS, 379, 297

Doi, Y., Takita, S., Ootsubo, T., et al. 2015, PASJ, 67, 50

Dokara, R., Brunthaler, A., Menten, K. M., et al. 2021, A&A, 651, A86

Dong, R., & Draine, B. T. 2011, ApJ, 727, 35

Downes, A. J. B., Salter, C. J., & Pauls, T. 1981, A&A, 97, 296

Downes, D., Wilson, T. L., Bieging, J., & Wink, J. 1980, A&AS, 40, 379

Draine, B., & Lazarian, A. 1998, ApJ, 508, 157

Draine, B. T. 2011, Physics of the Interstellar and Intergalactic Medium (Princeton, NJ: Princeton Univ. Press)

Du, X., Landecker, T. L., Robishaw, T., et al. 2016, PASP, 128, 115006

Dubner, G., & Giacani, E. 2015, A&ARv, 23, 3

Dulk, G. A., & Slee, O. B. 1975, ApJ, 199, 61

Dulk, P., & Slee, O. 1972, AuJPh, 25, 429

Dunkley, J., Amblard, A., Baccigalupi, C., et al. 2009, in AIP Conf. Proc. 1141, CMB Polarization Workshop: Theory and Foregrounds: CMBPol Mission Concept Study, ed. S. Dodelson et al. (Melville, NY: AIP), 222

Dupac, X., Bernard, J. P., Boudet, N., et al. 2003, A&A, 404, L11

Egron, E., Pellizzoni, A., Iacolina, M. N., et al. 2017, MNRAS, 470, 1329

Foreman-Mackey, D., Hogg, D. W., Lang, D., & Goodman, J. 2013a, PASP, 125, 306

Foreman-Mackey, D., Hogg, D. W., Lang, D., & Goodman, J. 2013b, PASP, 125, 306

Foss, M. K., Ihle, H. T., Borowska, J., et al. 2022, ApJ, 933, 184

Furst, E., Reich, W., Reich, P., & Reif, K. 1990, A&AS, 85, 691

Gao, X. Y., Reich, P., Hou, L. G., Reich, W., & Han, J. L. 2019, A&A, 623, A105

Génova-Santos, R., Rubiño-Martín, J. A., Peláez-Santos, A., et al. 2017, MNRAS, 464, 4107

GLIMPSE Team 2020, Galactic Legacy Infrared Midplane Survey Extraordinaire, IPAC Data Set

Goodman, J., & Weare, J. 2010, CAMCS, 5, 65

Gorski, K. M., Hivon, E., Banday, A. J., et al. 2005, ApJ, 622, 759

Goss, W. M., & Day, G. A. 1970, AuJPA, 13, 3

Goss, W. M., Skellern, D. J., Watkinson, A., & Shaver, P. A. 1979, A&A, 78, 75

Greaves, J. S., Scaife, A. M. M., Frayer, D. T., et al. 2018, NatAs, 2, 662

Green, A. J., Frail, D. A., Goss, W. M., & Otrupcek, R. 1997, AJ, 114, 2058

Green, D. A. 2009, MNRAS, 399, 177

Green, D. A. 2019, JApA, 40, 36

Habing, H. J., & Israel, F. P. 1979, ARA&A, 17, 345

Handa, T., Sofue, Y., Nakai, N., Hirabayashi, H., & Inoue, M. 1987, PASJ, 39, 709

Harper, S. E., Dickinson, C., Battye, R. A., et al. 2018, MNRAS, 478, 2416

Harper, S. E., Dickinson, C., & Cleary, K. 2015, MNRAS, 453, 3376

Harris, C. R., Millman, K. J., van der Walt, S. J., et al. 2020, Natur, 585, 357

Haslam, C. G. T., Salter, C. J., Stoffel, H., & Wilson, W. E. 1982, A&AS, 47, 1

Haynes, R., Caswell, J., & Simons, L. 1978, AuJPh, 31, 351

Hensley, B. S., & Draine, B. T. 2017, ApJ, 836, 179

Hensley, B. S., Draine, B. T., & Meisner, A. M. 2016, ApJ, 827, 45

Hensley, B. S., Murray, C. E., & Dodici, M. 2022, ApJ, 929, 23

Hoang, T., Vinh, N.-A., & Quynh Lan, N. 2016, ApJ, 824, 18

Hoare, M. G., Purcell, C. R., Churchwell, E. B., et al. 2012, PASP, 124, 939

Hoglund, B., & Mezger, P. G. 1965, Sci, 150, 339

Hughes, V. A., & Butler, R. 1969, ApJ, 155, 1061

Hunter, J. D. 2007, CSE, 9, 90

Irfan, M. O., Dickinson, C., Davies, R. D., et al. 2015, MNRAS, 448, 3572

Jonas, J. L., Baart, E. E., & Nicolson, G. D. 1998, MNRAS, 297, 977

Kalcheva, I. E., Hoare, M. G., Urquhart, J. S., et al. 2018, A&A, 615, A103

Kardashev, N. S. 1959, SvA, 3, 813

Karim, R. L., DeBoer, D., de Pater, I., & Keating, G. K. 2018, AJ, 155, 129

Kassim, N. E. 1992, AJ, 103, 943

Kellermann, K. I., Pauliny-Toth, I. I. K., & Williams, P. J. S. 1969, ApJ, 157, 1

Kesteven, M. J. L. 1968, AuJPh, 21, 739

Kuhn, M. A., de Souza, R. S., Krone-Martins, A., et al. 2021, ApJS, 254, 33

Kurtz, S. 2002, in ASP Conf. Ser. 267, Hot Star Workshop III: The Earliest Phases of Massive Star Birth, ed. P. Crowther (San Francisco, CA: ASP), 81

Kurtz, S., Churchwell, E., & Wood, D. O. S. 1994, ApJS, 91, 659

Lamb, J. W., Cleary, K. A., Woody, D. P., et al. 2022, ApJ, 933, 183

Landecker, T. L., Reich, W., Reid, R. I., et al. 2010, A&A, 520, A80

Leach, S. M., Cardoso, J. F., Baccigalupi, C., et al. 2008, A&A, 491, 597

Lee, E. J., Murray, N., & Rahman, M. 2012, ApJ, 752, 146

Li, T. Y., Wechsler, R. H., Devaraj, K., & Church, S. E. 2015, ApJ, 817, 169

Loru, S., Pellizzoni, A., Egron, E., et al. 2019, MNRAS, 482, 3857

Luisi, M., Anderson, L. D., Liu, B., et al. 2020, ApJ, 889, 96

Messineo, M., Menten, K. M., Figer, D. F., et al. 2014, A&A, 569, A20

Milne, D. K., & Hill, E. R. 1969, AuJPh, 22, 211

Miville-Deschenes, M., & Lagache, G. 2005, ApJS, 157, 302

Moffett, D. A., & Reynolds, S. P. 1994, ApJ, 425, 668

Molinari, S., Schisano, E., Elia, D., et al. 2016, A&A, 591, A149

Morsi, H. W., & Reich, W. 1987, A&AS, 69, 533

Murphy, T., Sadler, E. M., Ekers, R. D., et al. 2010, MNRAS, 402, 2403

Nguyen Luong, Q., Motte, F., Schuller, F., et al. 2011, A&A, 529, A41

Paladini, R., Burigana, C., Davies, R. D., et al. 2003, A&A, 397, 213

Pari, J., & Hora, J. L. 2020, PASP, 132, 054301

Pauliny-Toth, I. I. K., & Kellermann, K. I. 1966, ApJ, 146, 634

Peretto, N., & Fuller, G. A. 2009, A&A, 505, 405

Perrott, Y. C., Scaife, A. M. M., Green, D. A., et al. 2015, MNRAS, 453, 1396

Planck Collaboration, Abergel, A., Ade, P. A. R., et al. 2011, A&A, 536, A21

Planck Collaboration, Abergel, A., Ade, P. A. R., et al. 2014, A&A, 571, A11

Planck Collaboration, Ade, P. A. R., Aghanim, N., et al. 2014a, A&A, 571, A7

Planck Collaboration, Ade, P. A. R., Aghanim, N., et al. 2014b, A&A, 571, A9

Planck Collaboration, Ade, P. A. R., Aghanim, N., et al. 2014c, A&A, 571, A13

Planck Collaboration, Ade, P. A. R., Aghanim, N., et al. 2015, A&A, 580, A13

Planck Collaboration, Ade, P. A. R., Aghanim, N., et al. 2016a, A&A, 594, A25

Planck Collaboration, Ade, P. A. R., Aghanim, N., et al. 2018, A&A, 610, C1

Planck Collaboration, Aghanim, N., Ashdown, M., et al. 2016b, A&A, 596, A109

Planck Collaboration, Aghanim, N., Akrami, Y., et al. 2020, A&A, 641, A1

Planck Collaboration, Arnaud, M., Ashdown, M., et al. 2016c, A&A, 586, A134

Purcell, C. R., Hoare, M. G., Cotton, W. D., et al. 2013, ApJS, 205, 1

Reed, B. C. 2003, AJ, 125, 2531

Reich, P., & Reich, W. 1986, A&AS, 63, 205

Reich, W., Fuerst, E., Haslam, C. G. T., Steffen, P., & Reif, K. 1984, A&AS, 58, 197

Reich, W., Fuerst, E., Reich, P., & Reif, K. 1990, A&AS, 85, 633
Reifenstein, E. C., Wilson, T. L., Burke, B. F., Mezger, P. G., & Altenhoff, W. J. 1970, A&A, 4, 357
Rho, J., Petre, R., Schlegel, E. M., & Hester, J. J. 1994, ApJ, 430, 757
Rodgers, A. W., Campbell, C. T., & Whiteoak, J. B. 1960, MNRAS, 121, 103
Rohlfs, K., Wilson, T. L., & Hüttemeister, S. 2013, Tools of Radio Astronomy (6th ed.; Heidelberg: Springer)
Salter, C. J., Emerson, D. T., Steppe, H., & Thum, C. 1989a, A&A, 225, 167
Salter, C. J., Reynolds, S. P., Hogg, D. E., Payne, J. M., & Rhodes, P. J. 1989b, ApJ, 338, 171
Scaife, A., Green, D. A., Battye, R. A., et al. 2007, MNRAS, 377, L69
Scaife, A. M. M., Hurley-Walker, N., Davies, M. L., et al. 2008, MNRAS, 385, 809
Scaife, A. M. M., Green, D. A., Pooley, G. G., et al. 2010, MNRAS, 403, L46
Sharpless, S. 1959, ApJS, 4, 257
Shaver, P. A., & Goss, W. M. 1970, AuJPA, 14, 133
Silsbee, K., Ali-Haïmoud, Y., & Hirata, C. M. 2011, MNRAS, 411, 2750
Stevenson, M. A. 2014, ApJ, 781, 113
Strömgren, B. 1939, ApJ, 89, 526
Sun, X. H., Reich, P., Reich, W., et al. 2011, A&A, 536, A83
Sutton, D., Johnson, B. R., Brown, M. L., et al. 2009, MNRAS, 393, 894
Sutton, D., Zuntz, J. A., Ferreira, P. G., et al. 2010, MNRAS, 407, 1387
Takita, S., Doi, Y., Ootsubo, T., et al. 2015, PASJ, 67, 51

Taylor, A. R., Gibson, S. J., Peracaula, M., et al. 2003, AJ, 125, 3145
The Astropy Collaboration, Price-Whelan, A. M., Sipocz, B. M., et al. 2018, ApJ, 156, 123
The Astropy Collaboration, Robitaille, T. P., Tollerud, E. J., et al. 2013, A&A, 558, A33
Tibbs, C. T., Flagey, N., Paladini, R., et al. 2011, MNRAS, 418, 1889
Tibbs, C. T., Paladini, R., Cleary, K., et al. 2015, MNRAS, 453, 3356
Tibbs, C. T., Paladini, R., Compiègne, M., et al. 2012, ApJ, 754, 94
Tibbs, C. T., Watson, R. A., Dickinson, C., et al. 2010, MNRAS, 402, 1969
Todorovic, M., Davies, R. D., Dickinson, C., et al. 2010, MNRAS, 406, 1629
Tung, A. K., Kothes, R., Landecker, T. L., et al. 2017, AJ, 154, 156
Urošević, D. 2014, Ap&SS, 354, 541
Velusamy, T., & Kundu, M. R. 1974, A&A, 32, 375
Vidal, M., Casassus, S., Dickinson, C., et al. 2011, MNRAS, 414, 2424
Virtanen, P., Gommers, R., Oliphant, T. E., et al. 2020, NatMe, 17, 261
Watson, R. A., Rebolo, R., Rubiño-Martín, J. A., et al. 2005, ApJL, 624, L89
Weiland, J. L., Odegard, N., Hill, R. S., et al. 2011, ApJS, 192, 19
Yang, A. Y., Urquhart, J. S., Thompson, M. A., et al. 2021, A&A, 645, A110
Ysard, N., Juvela, M., & Verstraete, L. 2011, A&A, 535, A89
Zonca, A., Singer, L., Lenz, D., et al. 2020, Healpy: Python Wrapper for HEALPix, Astrophysics Source Code Library, ascl:2008.022
Zurita, A., Rozas, M., & Beckman, J. E. 2000, A&A, 363, 9